DOI: 10.1002/ejic.200600676

Redox Chemistry of a Dimanganese(II,III) Complex with an Unsymmetric Ligand: Water Binding, Deprotonation and Accumulative Light-Induced Oxidation

Magnus F. Anderlund,[a] Joakim Högblom,[b] Wei Shi,[a] Ping Huang,[a] Lars Eriksson,[c] Högni Weihe,[d] Stenbjörn Styring,[a] Björn Åkermark,[e] Reiner Lomoth,*[a] and Ann Magnuson*[a]

Keywords: Manganese / Bioinorganic chemistry / Ligand exchange / EPR spectroscopy / IR spectroscopy

A dinuclear manganese complex {[$Mn_2^{II,III}$L(μ-$OAc)_2$]-ClO_4} has been synthesised, where L is the dianion of 2-{[bis-(pyrid-2-ylmethyl)amino]methyl}-6-{[(3,5-di-*tert*-butyl-2-hydroxybenzyl)(pyrid-2-ylmethyl)amino]methyl}-4-methylphenol, an unsymmetric binucleating ligand with two coordinating phenol groups. The two manganese ions, with a Mn–Mn distance of 3.498 Å, are bridged by the two bidentate acetate ligands and the 4-methylphenolate group of the ligand, resulting in a N_3O_3 and N_2O_4 donor set of Mn^{II} and Mn^{III}, respectively. Electrochemically [$Mn_2^{II,III}$L(μ-$OAc)_2$]$^+$ is reduced to [$Mn_2^{II,II}$L(μ-$OAc)_2$] at $E_{1/2}(1)$ = –0.53 V versus $Fc^{+/0}$ and oxidised to [$Mn_2^{III,III}$L(μ-$OAc)_2$]$^{2+}$ at $E_{1/2}(2)$ = 0.38 V versus $Fc^{+/0}$. All three redox states have been characterised by EPR, IR and UV/Vis spectroscopy. Subsequent oxidation of [$Mn_2^{II,III}$L(μ-$OAc)_2$]$^{2+}$ [$E_{1/2}(3)$ = 0.75 V vs. $Fc^{+/0}$] in dry acetonitrile results in an unstable primary product with a lifetime of about 100 ms. At high scan rates quasireversible voltammetric behaviour is found for all three electrode processes, with particularly slow electron transfer for the II,III/II,II [$k°(1)$ = 0.002 cm s^{-1}] and III,III/II,III [$k°(2)$ = 0.005 cm s^{-1}] couples, which can be rationalised in terms of major distortions of the Mn^{III} centres. In aqueous media the bridging acetates are replaced by water-derived ligands. Deprotonation of these stabilises higher valence states, and photo-induced oxidation of the manganese complex results in a $Mn_2^{III,IV}$L complex with oxo or hydroxo bridging ligands, which is further oxidised to an EPR-silent product. These results demonstrate that a larger number of metal-centred oxidations can be compressed in a narrow potential range if build up of charge is avoided by charge-compensating reactions.

Introduction

The utilisation of solar energy for fuel production, through a molecular system for artificial photosynthesis, is an attractive solution to the need for renewable energy.[1] In natural photosynthesis, solar energy is used to extract electrons from water.[2] Photo-induced charge separation in the Photosystem II (PSII) reaction centre leads to oxidation of the water-oxidising complex (WOC), a catalyst consisting of a protein-bound cluster with four manganese ions and one calcium ion.[3,4] After four consecutive one-electron transfer events, the WOC retrieves four electrons from water and releases molecular oxygen.[3,5] During catalysis, the WOC cycles through five redox states.[6,7] The manganese ions are mostly in the Mn^{III} oxidation state or higher, and several of the intermediates involve manganese-centred oxidation.[7–9]

Synthetic manganese complexes have been extensively studied as model systems for the WOC but functional mimics that are able to evolve molecular oxygen from water are very few in number.[10,11] They require electrochemical oxidation at highly anodic potentials or strong chemical oxidants. In the latter case the formation of the important Mn-oxo intermediate often relies on oxygen atom transfer from the oxidant rather than from water.[11]

In our work towards artificial photosynthesis, we pursue supramolecular complexes in which the Mn portion undergoes accumulative oxidation by *light-induced* charge separation.[12–14] With the ultimate goal of photochemical water splitting, this requires Mn complexes that can un-

[a] Department of Photochemistry and Molecular Science, Uppsala University,
P. O. Box 523, 75120 Uppsala, Sweden
E-mail: ann.magnuson@fotomol.uu.se
reiner.lomoth@fotomol.uu.se
[b] Department of Biochemistry, Department of Chemistry, Lund University,
P. O. Box 124, 22100 Lund, Sweden
[c] Division of Structural Chemistry, Arrhenius Laboratories, Stockholm University,
10691 Stockholm, Sweden
[d] Department of Chemistry, University of Copenhagen,
Universitetsparken 5, 2100 Copenhagen, Denmark
[e] Department of Organic Chemistry, Arrhenius Laboratories, Stockholm University,
10691 Stockholm, Sweden
Supporting information for this article is available on the WWW under http://www.eurjic.org or from the author.

dergo four oxidation steps within the thermodynamic limit of the photo-oxidant. On the other hand, all stored oxidation equivalents need to be sufficiently oxidising, with an average potential of 0.8 V (at pH 7), to be capable of driving the catalytic oxidation of water.[15] In the WOC all four single-electron oxidations of the $Ca(Mn)_4$ cluster occur within an interval of only 0.25–0.3 V at potentials close to the limit (ca. 1 V vs. NHE[15]) given by the oxidising Tyr_Z radical. This compression of oxidation potentials is a result of charge-compensating deprotonation reactions and it is evident that a suitable mechanism for charge compensation is a central feature in the design of synthetic mimics.

In previous studies we could show that oxidation of the manganese dimer $[Mn_2(bpmp)(\mu\text{-}OAc)_2]^+$[16] in the presence of water involves exchange of the bridging acetates for water-derived ligands that are increasingly deprotonated in higher oxidation states.[17,18] The resulting charge compensation stabilises higher valence states and thereby allows for three metal-centred oxidations, from the $Mn_2^{II,II}$ dimer to a $Mn_2^{III,IV}$ species, to be driven by photo-generated $Ru^{II\text{-}I}(bpy)_3$.[13,17,19,20] The binding of water, deprotonation of bridging ligands and accumulative, light-induced oxidation of $[Mn_2(bpmp)(\mu\text{-}OAc)_2]^+$ mimic important aspects of the catalytic complex in PSII and we therefore set out to investigate modifications of the structural motif. With consideration to the prevalence of high-valent manganese species and the high O/N ratio in the ligand sphere of the $Ca(Mn)_4$ complex in PSII, we synthesised analogous dinuclear manganese complexes, with an increased number of phenolic ligand functions. In $[Mn_2(bhpp)(\mu\text{-}OAc)_2]^+$[19,21] two additional phenol groups of the bhpp ligand result in an oxygen-to-nitrogen ratio of 4:2. Compared to $[Mn_2(bpmp)(\mu\text{-}OAc)_2]^+$ with O/N = 3:3, the potentials for the manganese redox couples are lowered substantially and the oxidation equivalents stored on $[Mn_2(bhpp)(\mu\text{-}OAc)_2]^+$ are on average not sufficiently oxidising with respect to water oxidation.

In the present study we report a new di-μ-acetato-bridged dinuclear manganese complex, **5** ($[Mn_2L(\mu\text{-}OAc)_2]^+$), with an unsymmetric ligand molecule, L = 2-{[bis(pyrid-2-ylmethyl)amino]methyl}-6-{[(3,5-di-*tert*-butyl-2-hydroxybenzyl)(pyrid-2-ylmethyl)amino]methyl}-4-methylphenol. With a N_3O_3/N_2O_4 coordination sphere, the new complex is an intermediate between the $[Mn_2(bpmp)(\mu\text{-}OAc)_2]^+$ and $[Mn_2(bhpp)(\mu\text{-}OAc)_2]^+$ complexes. We chose to synthesise an unsymmetric ligand, as we anticipated that a compromise between the need for high valent Mn states and sufficiently high redox potentials could be accomplished with the intermediate O/N ratio. Here we present the synthesis and characterisation of the new manganese complex and its redox properties in anhydrous and partially aqueous solutions, including photo-oxidation studies.

Unsymmetric ligands have previously been used to a limited extent for coordinating manganese, mainly for mimicking the active site of manganese catalases,[22–25] or to support the formation of heterobinuclear metal complexes.[22,26] As a novelty in the present study, photo-oxidation of complex **5** generates products beyond the $Mn_2^{III,IV}$ level, which is not the case with $[Mn_2(bpmp)(\mu\text{-}OAc)_2]$, while the potentials are above those of $[Mn_2(bhpp)(\mu\text{-}OAc)_2]^+$. The favourable behaviour of the novel complex can be attributed to the combination of the flexible bridging motif that is inherent to this type of complex and the intermediate O/N ratio of the chelating ligand. These findings point to the intricate balance of donor properties in the set of permanent and flexible ligands that will be needed for functional mimics of the WOC suitable for photo-induced water oxidation.

Results and Discussion

Synthesis and Characterisation

Synthesis

The synthesis route for the preparation of compound **5** is described in Scheme 1. The synthesis of the unsymmetrical ligand H_2L (**4**) is based on the unsymmetrical phenol **1**.[27] Compound **2** was obtained by letting phenol **1** react with 1 equiv. of (3,5-di-*tert*-butyl-2-hydroxybenzyl)(2-pyridylmethyl)amine[21] and 2 equiv. of Et_3N in CH_2Cl_2 under reflux. Compound **3** was then obtained by reduction of **2** with $NaBH_4$ in methanol and thereafter chlorinated with $SOCl_2$ in dry CH_2Cl_2.

The unsymmetrical ligand H_2L (**4**) is produced by amination by nucleophilic attack on the benzylic chloride in **3** with bis-picolylamine[28] and Et_3N in CH_2Cl_2 under reflux. The yield was excellent in the first two steps (95.1 and 97.5%) but only moderate in the last step (67.4%), possibly because of steric hindrance of the two *tert*-butyl groups on the phenol.

The complexation of H_2L with $MnOAc_3{\cdot}2H_2O$ in ethanol under argon affords the stable dimanganese(II,III) complex **5** after addition of $NaClO_4{\cdot}H_2O$ in 52% yield. We have not been able to isolate any $Mn_2^{III,III}$ complex under these conditions. The reduction of Mn^{III} to Mn^{II} was possibly done by the solvent or by disproportionation of Mn^{III} to MnO_2 and Mn^{II} in the presence of water. Though we have not detected any MnO_2, we cannot rule out that colloidal MnO_2 was present in the solution after the complexation. However, the slow and well-behaved crystal growth, as well as the purity of the crystals established by elemental analysis, indicates that any impurities in the mother liquor were successfully removed prior to characterisation of **5**.

X-ray Structure Determination

The crystal structure of **5** (Figure 1) is of a monovalent cation, counterbalanced with a perchlorate ion (not shown). The displacement parameters of the perchlorate are heavily anisotropic, in agreement with a weakly coordinated perchlorate ion, and there are no ordered solvent molecules present in the structure. The manganese ions are bridged by the oxygen in the central 4-methylphenolate and the two bidentate acetates. The slightly distorted octahedral coordination of Mn(1) is completed by the two pyridyl nitrogen

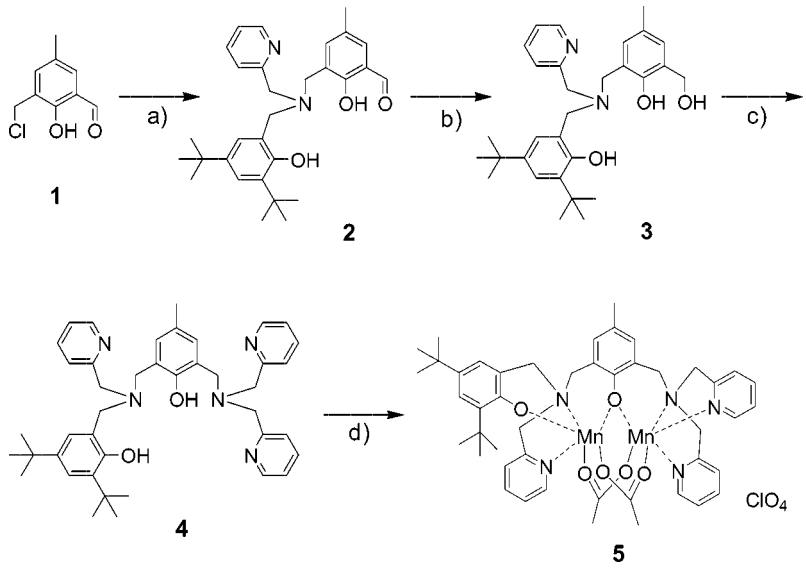

Scheme 1. Reaction conditions are as follows: (a) (3,5-di-*tert*-butylbenzyl-2-hydroxy)(2-pyridylmethyl)amine, CH_2Cl_2, reflux; (b) $NaBH_4$, MeOH, room temperature; (c) 1. $SOCl_2$, CH_2Cl_2, 2. DPA, Et_3N, CH_2Cl_2, reflux; (d) $MnOAc_3{\cdot}2H_2O$, EtOH, 60 °C, $NaClO_4{\cdot}H_2O$.

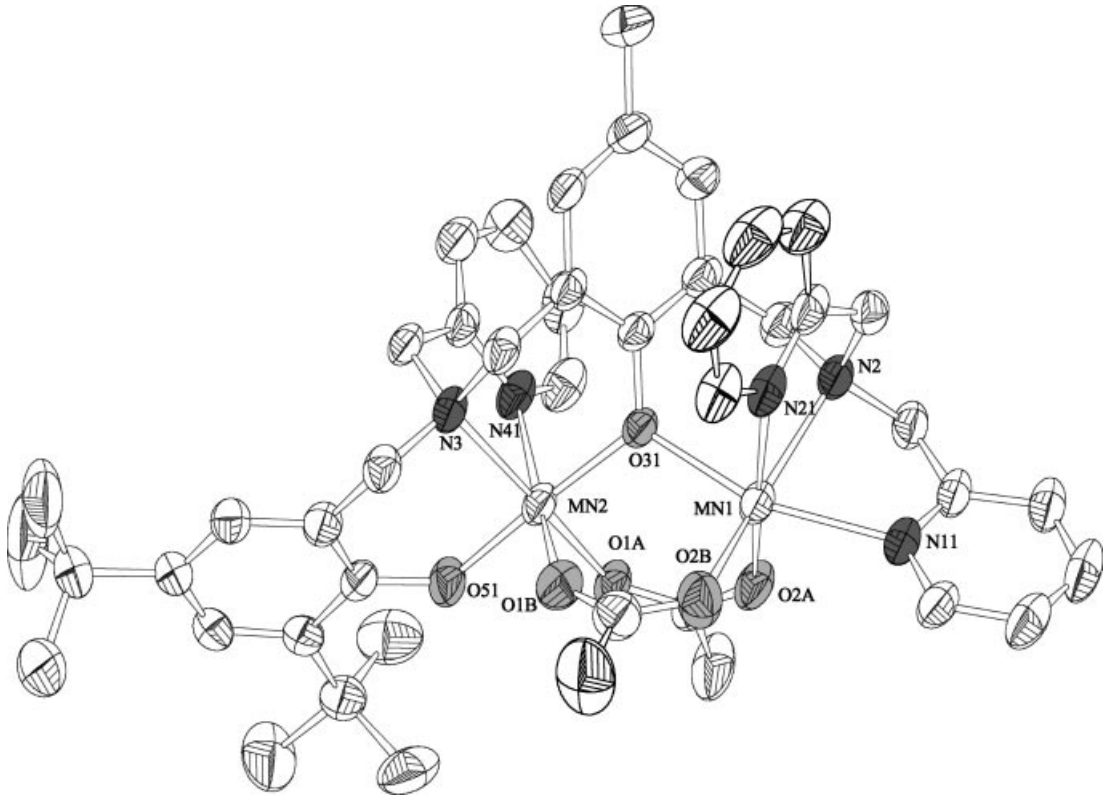

Figure 1. ORTEP view (30% probability ellipsoids) of **5** with atomic numbering for all non-hydrogen atoms. The hydrogen atoms were geometrically placed and shown as small circles of arbitrary radii. Figure drawn by Diamond.

atoms and one amine nitrogen atom of one branch of the ligand, resulting in a N_3O_3 ligand sphere. The oxygen atom from the *tert*-butyl-substituted phenolate coordinates Mn(2) in a *trans* position to the bridging phenolate group. The N_2O_4 coordination sphere of Mn(2) is completed by the pyridyl and amine nitrogens.

Selected bond lengths and angles are found in Table 1. Bond valence calculations gave 2.1 for Mn(1) and 3.2 for Mn(2) in agreement with the different donor sets and coordination symmetries of the two manganese ions.[29]

Mn(2) has a more distorted octahedral geometry, consistent with its assignment as Mn^{III}. For Mn(2), the shortest

Table 1. Selected bond lengths [Å] and angles [°] for **5**. The distances and angles given describe the coordination polyhedron around each Mn and the orientation of the two polyhedrons with respect to each other.

Mn1···Mn2	3.4985(15)	Mn1–O31–Mn2	116.95(18)
Mn1–O2b	2.089(5)	Mn2–O51	1.820(4)
Mn1–O2a	2.127(4)	Mn2–O31	1.922(4)
Mn1–O31	2.179(4)	Mn2–O1a	1.972(4)
Mn1–N11	2.255(5)	Mn2–N3	2.114(4)
Mn1–N21	2.280(5)	Mn2–O1b	2.154(5)
Mn1–N2	2.317(5)	Mn2–N41	2.266(6)
O2B–Mn1–O2A	99.6(2)	O51–Mn2–O31	177.1(2)
O2B–Mn1–O31	100.98(19)	O51–Mn2–O1A	86.47(18)
O2A–Mn1–O31	88.28(15)	O31–Mn2–O1A	92.05(16)
O2B–Mn1–N11	102.2(2)	O51–Mn2–N	89.93(18)
O2A–Mn1–N11	86.06(17)	O31–Mn2–N3	91.96(17)
O31–Mn1–N11	156.78(19)	O1A–Mn2–N3	169.45(18)
O2B–Mn1–N21	91.0(2)	O51–Mn2–O1B	89.5(2)
O2A–Mn1–N21	169.2(2)	O31–Mn2–O1B	88.16(19)
O31–Mn1–N21	87.68(15)	O1A–Mn2–O1B	97.3(2)
N11–Mn1–N21	93.77(18)	N3–Mn2–O1B	92.57(19)
O2B–Mn1–N2	164.6(2)	O51–Mn2–N41	96.5(2)
O2A–Mn1–N2	94.82(18)	O31–Mn2–N41	86.05(18)
O31–Mn1–N2	84.88(16)	O1A–Mn2–N41	92.22(19)
N11–Mn1–N2	73.20(19)	N3–Mn2–N41	78.33(19)
N21–Mn1–N2	74.9(2)	O1B–Mn2–N41	169.02(19)

Mn–O bond length is that of the *tert*-butyl-substituted phenoxyl (O51), and the bridging phenoxyl provides the second shortest Mn–O bond length. Thus, in contrast to the coordination sphere of Mn(1), the two bridging acetate ligands provide the longest Mn–O bonds. A similar, although less enhanced, effect was also observed for the Mn^{III} ion in the $[Mn_2^{II,III}(bpmp)(\mu\text{-}OAc)_2]^{2+}$ structure.[16] The ligand sphere of Mn(2) is therefore very compressed along the O–Mn–O axis, which is 0.21 Å shorter than the corresponding molecular axis of the Mn^{III} ion in $[Mn_2^{II,III}(bpmp)(\mu\text{-}OAc)_2]^{2+}$. The O–Mn–N axis formed by the pyridyl nitrogen and the carboxyl oxygen *trans* to it is quite long, making the Mn(2) coordination even more distorted, consistent with the Jahn–Teller effects that are common for Mn^{III} complexes. The Mn–Mn distance is 3.498 Å, and the Mn^{II}–O–Mn^{III} angle is 116.95°, which is in the range of other $Mn_2^{II,III}$ complexes.[16,25,30]

In conclusion, the crystal structure shows that the terminal phenoxyl in one branch of the ligand favours coordination of Mn^{III} over Mn^{II}, and that its axial position introduces an unusually large distortion away from octahedral symmetry.

Magnetic Susceptibility

The experimentally determined magnetic susceptibilities in the temperature range 4.45–301 K are shown in Figure 2. At room temperature, the effective magnetic moment is 7.20, which is slightly lower than the value 7.68 expected for a $Mn^{II}Mn^{III}$ dimer in which the metals are weakly antiferromagnetically interacting. The magnetic moment decreased smoothly from 298 K to 50 K, and then more abruptly down to 3 K. This behaviour is expected for an antiferromagnetically coupled $Mn_2^{II,III}$ complex with moderate exchange coupling.[16,30] At the lowest temperatures the magnetic moment was 1.79, which compares well with the value 1.73 expected for an $S = 1/2$ ground state.

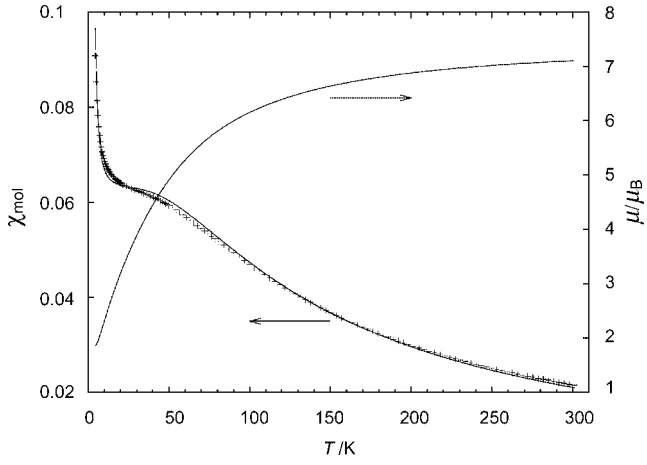

Figure 2. The magnetic susceptibility (+) and a fitted curve based on Equation (1) (solid line) in CGS units, as well as the effective magnetic moment as a function of temperature.

For known $Mn_2^{II,III}$ complexes the exchange coupling between the two manganese ions is rather weak, compared to that in $Mn_2^{III,IV}$ complexes, and typically ranges between about 0 and 10 cm^{-1}.[25,30,31] When analysing the susceptibility data for **5**, it proved impossible to satisfactorily interpret the magnetic susceptibilities in terms of an isotropic spin Hamiltonian (Model 1 in Table 2). As the zero-field splitting parameter D of Mn^{III} is often of the same order of magnitude as the exchange coupling J, the Hamiltonian was augmented with a term accounting for the magnetic anisotropy of the Mn^{III} ion,

$$H = J\,\hat{\mathbf{S}}_2\cdot\hat{\mathbf{S}}_3 + \mu_B\mathbf{B}\cdot\mathbf{g}\cdot(\hat{\mathbf{S}}_2 + \hat{\mathbf{S}}_3) + D_3[\hat{\mathbf{S}}^2_{3z} - \frac{1}{3}S(S+1)] \quad (1)$$

Table 2. Results from fitting magnetic susceptibility data. Models 1 and 2 refer to Equation (1) without and with the third term, respectively.

	Model 1	Model 2
J [cm^{-1}]	11.0 ± 0.05	10.9 ± 0.3
D_3 [cm^{-1}]	–	3.35 ± 0.4
TIP ($\times 10^{-12}$)	-5.05 ± 1.19	-3.95 ± 4.97
Curie ($\times 10^{-11}$)	4.04 ± 1.90	25 ± 4.5
χ^2	131.9	100
f-test	–	0.07
No. of fit parameters	3	4
Degrees of freedom	137	136
No. of points	140	140

In Equation (1) the subscripts refer to the oxidation numbers of the metal ions. By inclusion of the last term in Equation (1), the following parameters were obtained: $J = 10.9 \pm 0.3$ cm^{-1} and $D_3 = 3.35$ cm^{-1} (Model 2 in Table 2). The relatively large and positive zero-field parameter D_3 reflects to some degree the coordination geometry of the

Mn^{III} ion. Six-coordinated Mn^{III} complexes with distorted octahedral coordination typically display D values of –3 to –4 cm^{-1}. However, deviations occur, for example, when the ligand field has low symmetry in the equatorial plane, as in **5**, and the increased rhombicity of the ZFS parameters can lead to a change in sign to positive values of D.[32]

IR Spectroscopy

The IR spectrum of **5** in a KBr pellet was recorded between 4000 and 400 cm^{-1} (Supporting information). Based on characteristic frequencies the following assignments are suggested in agreement with the composition of the complex: 3062 (w, νC–H, aryl); 2952, 2867 (m, νC–H, alkyl); 1590 (s, ν_aC–O, carboxylate); 1441 (s, ν_sC–O, carboxylate); 1477, 1435 (s, νC–C, aryl); 1094 (s, ν_aCl–O, perchlorate); 623 (m, δ_aCl–O, perchlorate) cm^{-1}.

The IR spectrum of **5** in [D_3]acetonitrile solution (Supporting Information) is identical to the solid state spectrum, which provides strong evidence that the di-μ-acetato bridging structure established for crystalline **5** is maintained in anhydrous acetonitrile solution.

EPR Spectroscopy

The EPR spectrum of **5** in anhydrous acetonitrile is shown in Figure 3, spectrum a. The spectrum recorded at 4 K shows the $Mn_2^{II,III}$ S = 1/2 ground-state EPR signal, centred at g = 2 and displaying 16–20 hyperfine-lines, with a peak split of 110–140 gauss. The mixed-valence forms of dinuclear manganese complexes, $Mn_2^{II,III}$ and $Mn_2^{III,IV}$, are known to display similar ground-state EPR signals in the g = 2 region at cryogenic temperatures.[33] The acetato-bridged $Mn_2^{II,III}$ complexes normally show a weaker exchange coupling than μ-oxo-bridged $Mn_2^{III,IV}$ complexes, because of less orbital overlap between the Mn ions. The excited S = 3/2 and S = 5/2 states in the $Mn_2^{II,III}$ complexes will then give rise to transitions at low field, at relatively low temperatures (5–20 K). Thus, when the temperature was raised from 4 K to 5–11 K, the first excited state (S = 3/2) gave rise to a signal at g = 5.4 (Figure 3, inset).

The spectrum from complex **5** (Figure 3, a) could be simulated assuming an effective spin of S = 1/2, and using the spin Hamiltonian

$$\hat{H} = \beta\,\hat{\mathbf{S}}\cdot\mathbf{g}\cdot\mathbf{B} + \hat{\mathbf{I}}_1\cdot\mathbf{A}_1\cdot\hat{\mathbf{S}} + \hat{\mathbf{I}}_2\cdot\mathbf{A}_2\cdot\hat{\mathbf{S}} \quad (2)$$

(A full account of the EPR simulation parameters at both X- and Q-bands, as well as simulated spectra, was published by Huang et al.[34]) The obtained hyperfine tensors showed considerable anisotropy,[35] which could be explained by a significant Jahn–Teller distortion of Mn^{III}, taking into account the unexpected positive sign of the zero-field parameter D. These spectroscopic properties are a direct result of the rhombic distortion of the Mn^{III} coordination sphere.

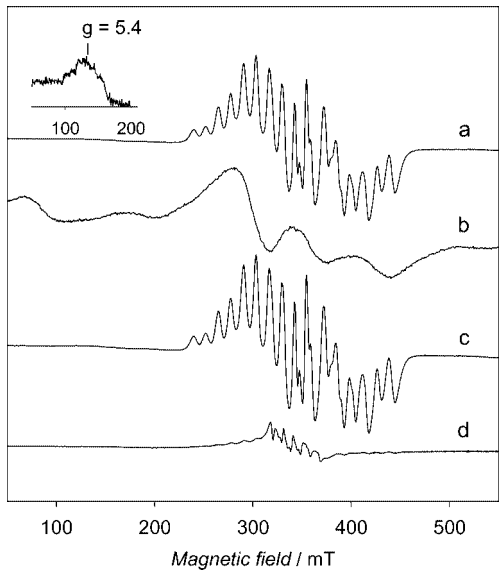

Figure 3. EPR spectra recorded by exposing **5** to controlled potentials. (a) After applying –0.08 V to the sample solution. The spectrum arises from the S = 1/2 ground spin state of the $Mn_2^{II,III}$ complex. No current was recorded at this potential. (b) After reduction at –0.93 V a spectrum typical of a weakly coupled $Mn_2^{II,II}$ complex is observed. (c) Recovery of the $Mn_2^{II,III}$ complex after reoxidation at –0.08 V of the sample giving spectrum b. (d) After oxidation at 0.57 V. The spectrum can be identified as a remaining fraction (5%) of $Mn_2^{II,III}$ complexes, still present after bulk electrolysis. In the centre of the spectrum, a six-line signal from monomeric Mn^{II} can be distinguished, corresponding to less than 2% of the manganese. Spectrometer settings: microwave frequency, 9.6 GHz; modulation amplitude, 10 G; microwave power spectrum a and c, 20 mW; in spectrum b, 2 mW; temperature in spectra a, c and d, 4 K; in spectrum b, 12 K. Insert: the signal at g = 5 arising from the excited S = 3/2 spin state of **5**, observed at $T > 5$ K.

Redox Properties in Anhydrous Media

Electrochemistry

The redox behaviour of **5** in acetonitrile was studied by cyclic voltammetry (CV), differential pulse voltammetry (DPV) and controlled potential electrolysis. The products of the oxidation and reduction processes were characterised by EPR spectroscopy and UV/Vis and IR spectroelectrochemisty. The electrochemical data are compiled in Table 3. All potentials are referenced versus ferrocene as redox standard and about 0.4 V should be added to these values in order to compare them with potentials in aqueous solution versus NHE.[36]

Voltammograms of **5** in acetonitrile solution (Figure 4) showed reversible to quasireversible CV waves for reduction at $E_{1/2}$ = –0.53 V (1) and oxidation at $E_{1/2}$ = 0.38 V versus Fc^+/Fc^0 (2) while further oxidation was irreversible on the normal CV time scale (v = 0.100 $V\,s^{-1}$). At higher scan rates on a microelectrode, the second oxidation gave rise to a quasireversible CV wave with the half-wave potential $E_{1/2}$ = 0.75 V (3) in good agreement with the DPV peak potential. Chemical reversibility was obtained for scan rates of $v \geq$ 10 $V\,s^{-1}$ and a lower limit of the lifetime of the product of the second oxidation of about 100 ms (at room tempera-

Table 3. Electrochemical data for $[Mn_2L(\mu\text{-}OAc)_2]^+$ in acetonitrile.

Redox process	(1)	(2)	(3)
Mn ox. states	II,III/II,II	III,III/II,III	–[a]
$E_{1/2}$[b] [V]	–0.535	0.380	0.755
$\Delta E_p(0.1)$[c,d] [mV]	70	100	–[e]
$\Delta E_p(100)$[c,f] [mV]	580	495	190
k°[f,g] [10^{-3} cm s^{-1}]	2	5	100

[a] Not assigned. [b] Half-wave potential ± 0.02 V vs. ferrocene/ferrocenium. [c] Peak split (scan rate in volts per second). [d] Glassy carbon electrode. [e] Irreversible at 0.1 V s^{-1}. [f] Pt microdisk electrode. [g] Apparent standard rate constant from digital simulation of cyclic voltammograms taking $\alpha = 0.5$ and $D = 1 \times 10^{-5}$ cm^2 s^{-1}.

ture) could be estimated. The reduction and the first oxidation of **5** are one-electron processes as evidenced by coulometry during controlled potential electrolysis at –0.93 and 0.57 V, respectively. We could not obtain reliable coulometric data for the second oxidation because of the instability of the product, but the voltammetric peak heights suggested the assignment to a one-electron process.[37]

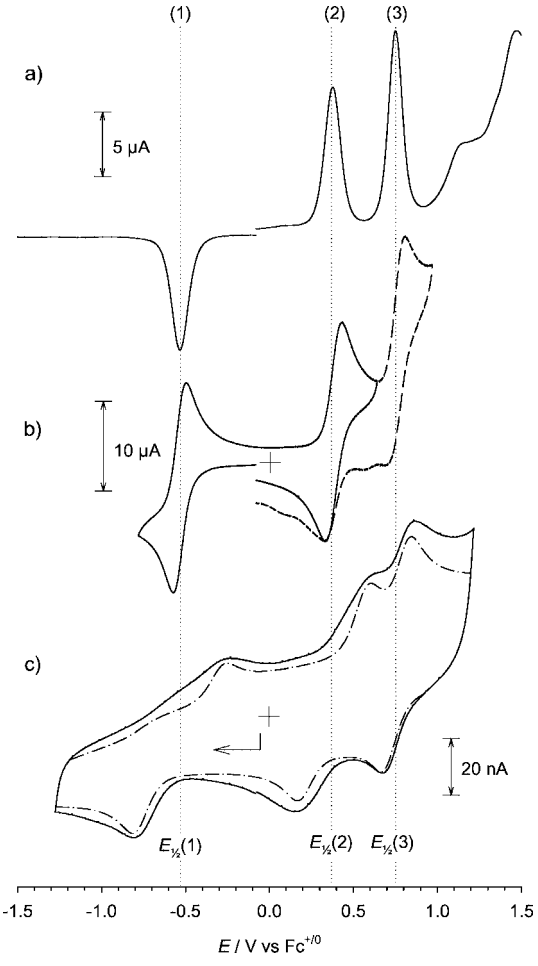

Figure 4. Voltammograms of **5** (1 mM) in acetonitrile with $(n\text{-}C_4H_9)_4N{\cdot}ClO_4$ (0.1 M) as supporting electrolyte. (a) Differential pulse voltammogram (step potential 5 mV, modulation amplitude 25 mV, modulation time 50 ms, interval time 100 ms, glassy carbon disk, 3 mm). (b) Cyclic voltammograms ($v = 0.100$ V s^{-1}, glassy carbon disk, 3 mm). (c) Cyclic voltammogram ($v = 100$ V s^{-1}, Pt microdisk, 25 μm) and digital simulation (– · –) with the parameters from Table 1.

The electrode processes (1) and (2) exhibited much larger CV peak splits at high scan rates than process (3) (Figure 4). This strongly non-Nernstian behaviour is indicative of slow heterogeneous electron transfer. We could obtain the standard rate constants k° to a close approximation by digital simulations (Figure 4, c) using a model of three quasireversible waves and the parameters given in Table 3. Neglecting work terms, the standard rate constant for a heterogeneous electron transfer reaction is given by

$$k^\circ = Z_{het}\left\{e^{-\lambda/(4kT)}\right\} \quad (3)$$

where Z_{het} is the collision factor and λ is the reorganisation energy.[38] For **5** we obtain

$$Z_{het} = (RT/2\pi M)^{1/2} = 2.2 \times 10^3 \text{ cm s}^{-1} \quad (4)$$

($M = 883$ g mol^{-1}) and can estimate approximate reorganisation energies of 1.4, 1.3 and 1.0 eV for the electrode processes (1), (2) and (3), respectively. The contribution of the solvent reorganisation can be estimated as $\lambda_{solv} \leq 0.3$ eV.[39] This would indicate that the electrode reactions, in particular (1) and (2), are associated with large inner reorganisation energies of $\lambda_i \approx 1$ eV. A similar estimate of λ_i based on crystallographic data for the II,III/II,II couple of $[Mn_2(bpmp)(\mu\text{-}OAc)_2]^{2+/+}$ has been presented and can explain the unusually slow electron transfer observed in electron transfer dyads and triads that involve manganese complexes as donor units.[14,40] For the Mn^{II}/Mn^{III} couples this can be attributed to the Jahn–Teller distortion associated with the high-spin d^4 configuration of the Mn^{III} centre. The significantly smaller reorganisation energy for the second oxidation implies that the coordination geometry changes are less pronounced between Mn^{III} and Mn^{IV} or that this process is a ligand-based rather than a metal-centred oxidation.

Spectroscopic Characterisation of the Oxidation and Reduction Products

The one-electron reduction product was prepared by bulk electrolysis at –0.93 V. Its EPR spectrum (Figure 3b) is typical for a weakly antiferromagnetically coupled $Mn_2^{II,II}$ complex and the reduction of **5** can be attributed to the metal-centred process (5).

$$[Mn_2^{II,III}L(\mu\text{-}OAc)_2]^+ + e^- \rightarrow [Mn_2^{II,II}L(\mu\text{-}OAc)_2] \quad (5)$$

$Mn_2^{II,II}$ is an integral spin system, where the diamagnetic ($S = 0$) ground state dominates at liquid He temperatures and accordingly we did not detect any EPR signals at 4 K. Weakly coupled $Mn_2^{II,II}$ complexes are, on the other hand, known to display EPR-active excited states at temperatures above about 7 K, similar to that in Figure 3, spectrum b.[41] We therefore conclude that the spectrum in Figure 3 (b), which was recorded at 12 K, originates from a superposition of one or more excited spin states from $Mn_2^{II,II}$ with $S = 1, 2, \ldots$. When $[Mn^{II}{}_2L(\mu\text{-}OAc)_2]$ was reoxidised by elec-

trolysis at –0.08 V, the $Mn_2^{II,III}$ spectrum of **5** was quantitatively recovered (Figure 3, c), confirming the stability of $[Mn^{II}{}_2L(\mu\text{-}OAc)_2]$.

The one-electron oxidation product was produced by bulk electrolysis at 0.57 V. The product is EPR-silent and the spectrum only showed a residual (5%) of the original $Mn_2^{II,III}$ signal (Figure 3, d). $Mn_2^{III,III}$, which is an integral spin system, might produce EPR-active states at higher temperatures, but so far no EPR signals from this valence state in either parallel or perpendicular mode EPR at X-band frequencies have been found by us or other researchers. Therefore, the EPR-silent product of the first oxidation can be assigned to$[Mn_2^{III,III}L(\mu\text{-}OAc)_2]^{2+}$ according to equation (6).

$$[Mn_2^{II,III}L(\mu\text{-}OAc)_2]^{+} \rightarrow [Mn_2^{III,III}L(\mu\text{-}OAc)_2]^{2+} + e^- \quad (6)$$

After reduction of $[Mn_2^{III,III}L(\mu\text{-}OAc)_2]^{2+}$at –0.08 V about 95% of the original $Mn_2^{II,III}$ signal was recovered (not shown). A slow degradation reaction of $[Mn_2^{III,III}L(\mu\text{-}OAc)_2]^{2+}$ resulted in the release of minor amounts of monomeric Mn^{II} that could be observed in the spectra of the oxidised and re-reduced material (2% and 5% of the total Mn respectively), where it gave rise to the weak EPR signal around $g = 2$ with six hyperfine lines at a separation of about 100 gauss (Figure 4, d).

The short-lived primary product of the second oxidation could not be prepared by bulk electrolysis. After electrolysis at 0.82 V a significant amount of monomeric Mn^{II} was observed by EPR, obscuring any other paramagnetic species that might be present in the solution (not shown). The instability of the oxidised complex on longer timescales can be attributed to oxidative degradation of the ligand, as evidenced by the release of monomeric Mn^{II} ions. This reaction might be triggered either by a transiently formed high-valent metal centre (7a) or by direct ligand oxidation (7b).

$$[Mn_2^{III,III}L(\mu\text{-}OAc)_2]^{2+} \rightarrow [Mn_2^{III,IV}L(\mu\text{-}OAc)_2]^{3+} + e^- \quad (7a)$$

$$[Mn_2^{III,III}L(\mu\text{-}OAc)_2]^{2+} \rightarrow [Mn_2^{III,III}L^{\cdot}(\mu\text{-}OAc)_2]^{3+} + e^- \quad (7b)$$

UV/Vis Spectroelectrochemistry

The electronic absorption spectra of $[Mn_2L(\mu\text{-}OAc)_2]^{n+}$ ($n = 0, 1, 2$) in the UV and visible range are shown in Figure 5 and Table 4. The spectra after one-electron reduction and one-electron oxidisation of **5** were obtained by spectroelectrochemistry. The spectral changes induced by reduction and the first oxidation were fully reversible and isosbestic points (221, 242, 260, 306, 332 nm) were maintained in the course of the reduction (Figure 5, left panel). In the $Mn_2^{II,II}$ state the complex displayed basically no visible absorption as metal-to-ligand charge transfer (MLCT) bands of Mn^{II} complexes are usually of low intensity. The visible absorption bands of the $Mn_2^{II,III}$ and $Mn_2^{III,III}$ states (Figure 5, right panel) can be attributed to ligand-to-metal charge transfer (LMCT) transitions from multiple donor functions to the Mn^{III} centres. No additional band of the mixed-valence complex could be detected including the near infrared spectrum ($\leq$ 2700 nm). With a free energy change of $\Delta G° \approx 0.5$ eV for the metal-to-metal charge transfer (8) and $\lambda > 1$ eV per metal centre, the intervalence charge transfer transitions might be superimposed on the LMCT bands in the UV/Vis range.

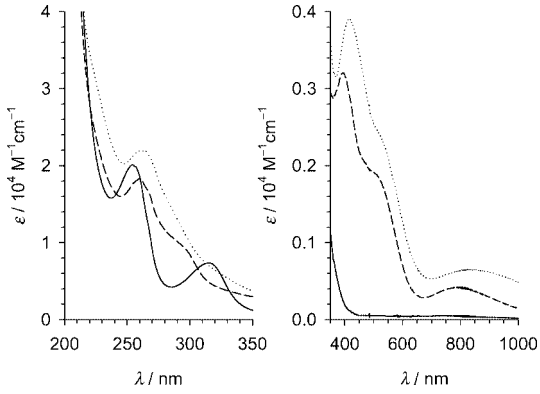

Figure 5. Electronic spectra of $[Mn_2L(\mu\text{-}OAc)_2]$ (–), $[Mn_2L(\mu\text{-}OAc)_2]^{+}$ (– –) and $[Mn_2L(\mu\text{-}OAc)_2]^{2+}$ (· · ·) in acetonitrile with $(n\text{-}C_4H_9)_4N{\cdot}ClO_4$ (0.1 M).

Table 4. UV/Vis absorption data of $[Mn_2L(\mu\text{-}OAc)_2]^{n+}$ in acetonitrile.

n	Mn oxidation state	λ_{max} [nm] (ε [$M^{-1}cm^{-1}$])
0	II,II	202 (61200), 253 (20100), 315 (7350)
1	II,III	260 (18300), 393 (3200), 795 (420)
2	III,III	262 (22000), 417 (3900), 830 (650)

$$[(N)_3Mn^{II}(\mu\text{-}O\text{-}\phi)(\mu\text{-}OAc)_2Mn^{III}(N)_2(O)] \rightarrow [(N)_3Mn^{III}(\mu\text{-}O\text{-}\phi)(\mu\text{-}OAc)_2Mn^{II}(N)_2(O)] \quad (8)$$

Upon the second oxidation the optical absorption above 377 nm and below 310 nm was bleached and an increasing absorption was initially observed between these wavelengths. The isosbestic points were, however, not maintained and a pure spectrum of the initial product could not be obtained.

Scheme 2 compares the redox properties of **5** to those of the symmetric analogues $[Mn_2(bpmp)(\mu\text{-}OAc)_2]^{+}$ and $[Mn_2(bhpp)(\mu\text{-}OAc)_2]^{+}$ with $(N_3O_3)_2$ and $(N_2O_4)_2$ donor sets, respectively.[17,21] It illustrates the stabilisation of high-valent metal centres by the increasing number of oxygen donors. For the unsymmetric complex the mixed $(N_3O_3)/(N_2O_4)$ donor set results in localisation of and an extended stability to the mixed-valence $Mn_2^{II,III}$ state, with a free energy of comproportionation of $\Delta G_c = -88$ kJ mol^{-1} [$K_c = \exp(\Delta E_{1/2}F/RT) = 5.49 \times 10^{15}$ at 293 K] as compared to –54.0 and –34.7 kJ mol^{-1} in the $(N_3O_3)_2$ and $(N_2O_4)_2$ ana-

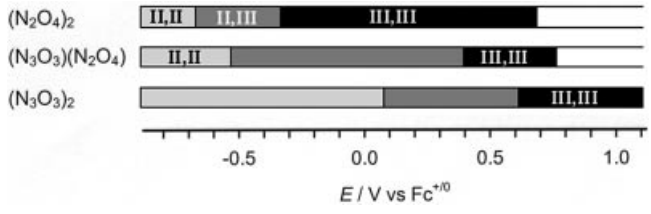

Scheme 2.

logues, respectively. For **5**, as for the symmetric analogues, no metal oxidation state higher than $Mn_2^{III,III}$ could be obtained by bulk electrolysis in nonaqueous solvents, and the second oxidation of **5** resulted in a short-lived product that could not be characterised. This demonstrates the general problem that several accumulative oxidations without charge compensation will be spread over a large potential range, placing the potentials for generating the higher metal oxidation states so high that oxidative degradation of the complexes is inevitable.

IR Spectroelectrochemistry

IR spectra of the isovalent complexes $[Mn_2^{II,II}L(\mu\text{-}OAc)_2]$ and $[Mn_2^{III,III}L(\mu\text{-}OAc)_2]^{2+}$ (see Supporting Information) were obtained by spectroelectrochemistry that gave fully reversible absorption changes for reduction and oxidation of **5**. For the ν_{as} mode of the acetate ligands only a minor shift to higher frequency is observed upon reduction, while oxidation results in a broader, less symmetric ν_{as} band. The absorption between 1440 and 1440 cm^{-1} can be assigned to the ν_s mode of the acetate ligands superimposed on absorptions of the binucleating ligand. The spectral changes induced by reduction and oxidation suggest a shift towards higher frequency in the II,II state and to lower frequency in the III,III state. The same trend has been found for the $Mn_2(bpmp)(\mu\text{-}OAc)_2$ complex[18] and the values of $\Delta\tilde{\nu} = \tilde{\nu}_{as} - \tilde{\nu}_s$ of about 120, 170 and 220 cm^{-1} would be in agreement with bridging coordination of the acetate in all three oxidation states.

Redox Properties in Partially Aqueous Media

In previous studies of $[Mn_2(bpmp)(\mu\text{-}OAc)_2]^+$ and $[Mn_2(bhpp)(\mu\text{-}OAc)_2]^+$, we have shown that complexes in higher oxidation states can be generated in partially aqueous solutions.[17–19] For $[Mn_2(bpmp)(\mu\text{-}OAc)_2]^+$ we could show that the exchange of acetate bridges for water-derived ligands (H_2O, OH^-, O^{2-}) accounts for the changes in redox behaviour in the presence of water. We were able to identify the products of the ligand exchange reactions and could demonstrate that increasing deprotonation of water-derived ligands provides the charge compensation needed for the stabilisation of high metal oxidation states.[18] In this way a di-μ-oxo-bridged dimer $[Mn_2^{III,IV}(bpmp)(\mu\text{-}O)_2]^{2+}$ can be obtained by three-electron oxidation of $[Mn_2^{II,II}(bpmp)(\mu\text{-}OAc)_2]^+$ that cannot be oxidised beyond the $Mn_2^{III,III}$ state, in its original di-μ-acetato form.

It could be anticipated that similar ligand exchange processes might take place in **5**. We therefore wanted to investigate the extent of these processes in **5**, and if complexes with oxidation states higher than $Mn_2^{III,III}$ could be formed from **5** as a result of ligand exchange in aqueous media.

IR Spectroscopy

The exchange of acetate ligands for water-derived ligands was monitored by IR spectroscopy in CD_3CN/D_2O mixtures (Figure 6, a). With increasing water concentration the sharp absorption peak arising from the acetate ligands (ν_{as}, 1590 cm^{-1}, ε = 4170 $M^{-1}cm^{-1}$) is depleted and replaced by the broader and weaker ν_{as} band of free acetate ions that can be observed at lower frequency (1574 cm^{-1}, ε = 840 $M^{-1}cm^{-1}$).[18] The ratio of free versus bound acetate approaches unity, indicating that on average only one acetate per molecule of **5** is lost, even for the highest water concentration (inset in Figure 6, a). Assuming that the absorption changes represent a uniform reaction, this indicates that either all complexes have lost one acetate or half of them have lost both ligands. The dependence of the acetate concentration on the water content (Figure 6, b) is in good agreement with (9), with an equilibrium constant K_9 = 7.6×10^{-5} M^{-1} (Figure 6, c), while other obvious possibilities (10, 11) are not in agreement with the IR data.

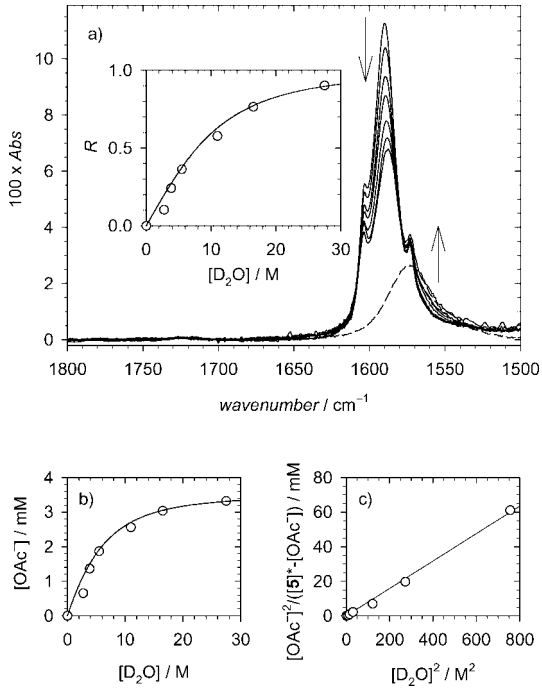

Figure 6. (a) IR spectra of **5** (3.5 mM) in $[D_3]$acetonitrile and $[D_3]$-acetonitrile/water (D_2O) mixtures. Arrows indicate direction of absorbance changes for increasing D_2O concentration. Dashed line is the spectrum of ionic acetate (3.5 mM as NaOAc). Inset: ratio R = $[OAc^-]/[M\text{-}OAc]$ of ionic vs. coordinated acetate as a function of water concentration. (b) Absolute concentration of ionic acetate and (c) plot according to Reaction (9) with a slope of K_9 = 7.6×10^{-5} M^{-1}. [Lines in (a) inset and (b) are computed with this value of K_9.]

$$[Mn_2L(\mu\text{-}OAc)_2]^+ + 2H_2O \leftrightarrows [Mn_2L(\mu\text{-}OAc)(H_2O)_2]^{2+} + OAc^- \quad (9)$$

$$[Mn_2L(\mu\text{-}OAc)_2]^+ + H_2O \leftrightarrows [Mn_2L(\mu\text{-}OAc)(\mu\text{-}H_2O)]^{2+} + OAc^- \quad (10)$$

$$[Mn_2L(\mu\text{-}OAc)_2]^+ + 2H_2O \leftrightarrows [Mn_2L(\mu\text{-}H_2O)_2]^{3+} + 2OAc^- \quad (11)$$

In summary, the IR data suggest that one of the acetate bridges is lost more readily and is replaced by two terminal aquo ligands while the second acetate remains coordinated to the Mn centres even at the highest water concentrations. In this respect **5** behaves differently from the bpmp ana-

logues where the $Mn_2^{II,II}$ complex, which has the same charge as **5**, as well as the $Mn_2^{II,III}$ complex, in the same valence state as **5**, release both acetate ligands under comparable conditions.[18] Another difference between **5** and $[Mn_2(bpmp)(\mu\text{-}OAc)_2]^{2+}$ is the protonation state of the water-derived ligands. For the bpmp complex it was observed that the reaction of the $Mn_2^{II,III}$ state with water results in free acetate as well as acetic acid, which can be rationalised in terms of deprotonation of the water-derived ligands, resulting in the formation of oxo- and hydroxo bridges. In the case of **5** the absence of acetic acid hence implies that the aquo ligands are less acidic and remain protonated when bound to the $Mn_2^{II,III}$ complex. It is therefore likely that the water-derived ligands are terminal and not bridging in this valence state, although the formation of bridging aqueous ligands cannot be ruled out.

Electrochemistry

The effect of the ligand exchange reactions on the redox behaviour of **5** was studied by cyclic voltammetry in different acetonitrile/water mixtures (Figure 7). With lower water concentration (1% v:v, 0.55 M) the ligand exchange equilibrium is largely on the left hand side and the magnitude of the first oxidation wave (2) is identical to dry acetonitrile solution (Figure 7, a and b). Also the reversibility of this wave (2) as well as the magnitude and reversibility of the reduction wave (1) (not shown) are unaffected. This indicates that under these conditions **5** does not react with water to a sizeable extent neither in the initial $Mn_2^{II,III}$ nor in the $Mn_2^{III,III}$ or $Mn_2^{II,II}$ forms.

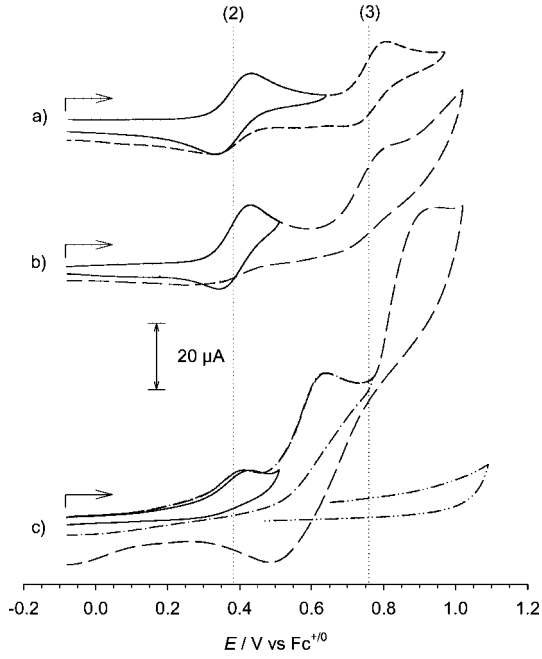

Figure 7. Cyclic voltammograms (v = 0.100 V s^{-1}, first scans) of **5** (1 mM) with (n-$C_4H_9)_4N{\cdot}ClO_4$ (0.1 M) as supporting electrolyte. (a) Anhydrous acetonitrile. (b) Acetonitrile with 1% water (v:v). (c) Acetonitrile with 10% water (v:v). The dashed and dotted line shows the solvent background with 10% water.

With higher water concentration (10% v:v, 5.5 M) the first oxidation wave (2) is already depleted and fully irreversible while the second oxidation wave (3) of the original complex is absent (Figure 7, c). This shows that with the increased water content more than half of the complexes react with water already in the initial $Mn_2^{II,III}$ state, and the more reactive $Mn_2^{III,III}$ state is converted completely by the ligand exchange reactions. The additional anodic peaks around 0.6 and 0.9 V can be attributed to the oxidation of the products from the ligand exchange reactions. The first attempts to investigate the ligand exchanged oxidation products by EPR spectroscopy after bulk electrolysis of **5** in partially aqueous solutions were unsuccessful however. We therefore sought information on the oxidation products from IR spectroscopy, which benefits from more rapid electrochemical conversion in the thin-layer cell employed for IR spectroelectrochemistry.

IR Spectroelectrochemistry

Figure 8 shows the IR absorption changes induced by oxidation of **5** in acetonitrile solution with 10% water. Electrolysis at the potential of the first oxidation (0.47 V vs. $Fc^{+/0}$) generates acetic acid (1725, 1380 and 1300 cm^{-1}) as well as free acetate ions with their absorption band (1575 cm^{-1}) partly cancelled by the bleach of the acetate ligand band (1590 cm^{-1}). This is in line with the notion that higher oxidation states are more reactive towards water (see Electrochemistry) and demonstrates that the water-derived ligands are at least partly deprotonated upon oxidation of the Mn centres. Subsequent oxidation at 0.72 V versus $Fc^{+/0}$ transforms the remaining acetate ligands as well as the acetate released in the previous oxidation step into acetic acid. This shows that the product(s) generated in the second oxidation wave peaking at 0.6 V do not carry any acetate ligands and that the water-derived ligands are further deprotonated.

Therefore, it can be concluded that the most oxidised products are oxo- ore hydroxo-bridged complexes. For $[Mn_2^{II,II}(bpmp)(\mu\text{-}OAc)_2]^+$ we showed that $[Mn_2^{III,IV}(bpmp)(\mu\text{-}O)_2]^{2+}$ was formed close to the potential of the III,III/II,III couple of the parent complex. The product was identified by rapid on-line transfer of the electrolysis products to a mass spectrometer.[18] The same product complex was also detected by EPR spectroscopy after light-induced oxidation of $[Mn_2^{II,II}(bpmp)(\mu\text{-}OAc)_2]^+$ via $[Ru^{III}(bpy)_3]^{3+}$ and rapid freezing of the products.[17,19] With the increased O/N ratio of complex **5** we anticipated that product complexes at least at the $Mn_2^{III,IV}$ level or even higher might be formed with the Ru^{III} oxidant ($E_{1/2}$ = 0.90 V vs. $Fc^{+/0}$) and be detected by a combination of photo-oxidation and EPR spectroscopy.

EPR Spectroscopy of Photo-Oxidised Samples

The oxidant $[Ru^{III}(bpy)_3]^{3+}$ was generated by oxidative quenching of photoexcited $[Ru^{II}(bpy)_3]^{2+}$. The sacrificial electron acceptor $[Co^{III}(NH_3)_5Cl]^{2+}$ avoids electron recombination, and thereby allows for accumulative oxidation of the manganese complex. To dissolve a sufficient amount of

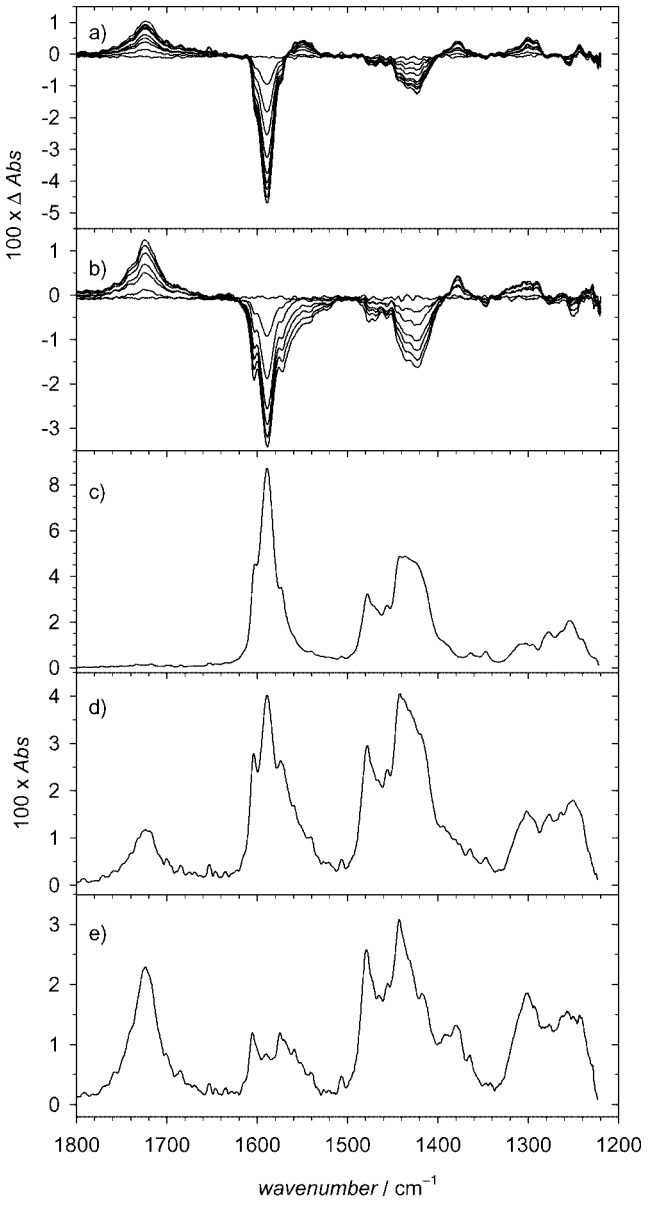

Figure 8. IR spectroelectrochemistry of **5** (3.5 mM) in [D_3]acetonitrile with 5.5 M water (D_2O). Absorbance changes upon oxidation at 0.47 V vs. $Fc^{+/0}$ (a) and subsequent oxidation at 0.72 V vs. $Fc^{+/0}$ (b). Spectra before oxidation (c) and after exhaustive oxidation at 0.47 V (d) and 0.72 V (e).

the acceptor, a high water content (1:1 water/acetonitrile) was needed for these measurements. The results from the IR spectra demonstrate that under these conditions each complex loses one of the acetate ligands already in the initial $Mn_2^{II,III}$ state. When **5** was dissolved in the reaction mixture, the 17 hyperfine lines in the $Mn_2^{II,III}$ EPR spectrum were broadened, and a signal with less-resolved hyperfine structure dominated the spectrum of the starting material (Figure 9, spectrum a). However, the integrated area of the spectrum was almost the same as for the well-resolved $Mn_2^{II,III}$ spectrum in acetonitrile (the magnitude of the EPR signal corresponds to about 80% of the nominal concentration), which indicates that essentially the entire sample remained in the original valence state. This demonstrates that even at this very high water content the major part of the material prevails as coupled $Mn_2^{II,III}$ dimers, and the broadened hyperfine structure can be attributed to strain effects due to accessibility to the bulk solution.

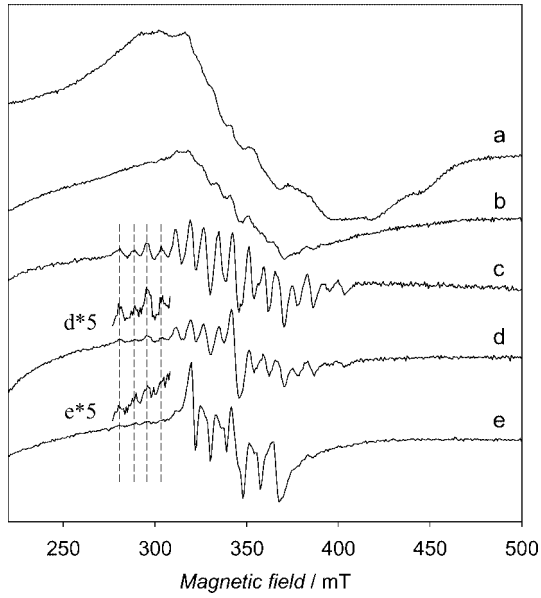

Figure 9. EPR spectra of **5** (0.5 mM) exposed to a variable number of laser flashes at 20 °C in the presence of $[Ru^{II}(bpy)_3]^{2+}$ (4 mM) and $[Co^{III}(NH_3)_5Cl]^{2+}$ (8 mM) in acetonitrile/aqueous solution (1:1 v/v). The spectra were recorded from the same sample, exposed to 0 (a), 20 (b), 100 (c), 180 (d) and 380 (e) laser flashes. In spectra d and e the magnified parts on the low-field side show the remaining presence of the EPR signal from $Mn_2^{III,IV}$. Spectrometer settings as in Figure 4.

Upon illumination with an increasing number of laser flashes, the initial EPR signal from $Mn_2^{II,III}$ decreased successively (Figure 10). To ensure accurate quantification of $Mn_2^{II,III}$, all measurements were made at 4 K, where all complexes are in the $S = 1/2$ ground state.[36] The simultaneously increasing EPR signal from the reduced electron acceptor $[Co^{II}(NH_3)_x(H_2O)_y]^{2+}$ ($g = 5$, not shown but cf. Huang et al.[17]) showed that the depletion of the $Mn_2^{II,III}$ signal is due to oxidation with the photogenerated $[Ru^{III}(bpy)_3]^{3+}$.

After 40 flashes a new signal at $g = 2$ appeared (Figure 9, spectrum c). It bears the typical signatures of a $S = 1/2$ ground state of a strongly coupled $Mn_2^{III,IV}$ complex, being about 2300 gauss wide and displaying 16 hyperfine lines with a spacing of 75–80 gauss.[34,42] The hyperfine splitting arises because of strong antiferromagnetic coupling typical of di-μ-oxo- or di-μ-hydroxo-bridged $Mn_2^{III,IV}$ dimers. For $[Mn_2(bpmp)(\mu\text{-}OAc)_2]^+$ we could demonstrate that the aquo and hydroxo complexes formed by ligand exchange in the lower oxidation states were ultimately transformed into the di-μ-oxo complex upon oxidation to the $Mn_2^{III,IV}$ level.[18] With the additional phenolate donor ligand in **5**, a μ-oxo-μ-hydroxo complex is the most probable structure for this oxidation state.

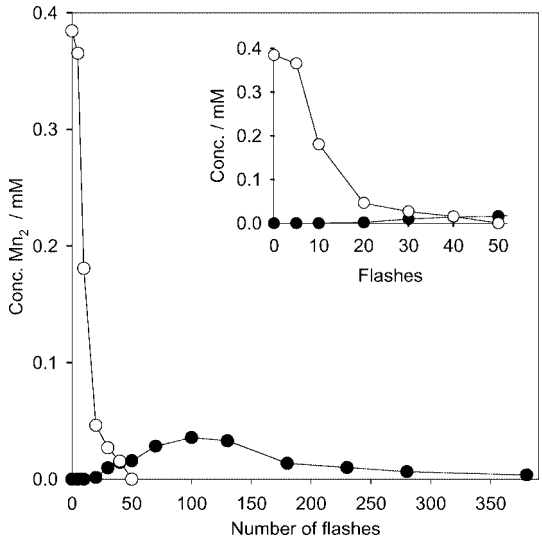

Figure 10. Flash-dependent concentrations of $Mn_2^{II,III}$ (–○–) and $Mn_2^{III,IV}$ (–●–). The data are obtained after quantification of $Mn_2^{II,III}$ and $Mn_2^{III,IV}$ from EPR spectra similar to those in Figure 7. All $Mn_2^{II,III}$ is quantitatively oxidised after 50 flashes, and the maximum observed amount of $Mn_2^{III,IV}$ appears after 100 flashes. The intermediate, $Mn_2^{III,III}$, cannot be observed by EPR. The inset shows a magnification of the data obtained between flashes 0 and 50, to highlight the lag phase in formation of $Mn_2^{III,IV}$.

Oxidation of the $Mn_2^{II,III}$ complexes to the $Mn_2^{III,IV}$ product with the one-electron photo-oxidant $Ru^{III}(bpy)_3$ should proceed via intermediates at the $Mn_2^{III,III}$ level. These are expected to be EPR-silent and not observable by EPR, which explains the lag phase between complete disappearance of the $Mn_2^{II,III}$ EPR spectrum and the maximum intensity of the $Mn_2^{III,IV}$ EPR signal (Figure 10). After 40 flashes, approximately equal concentrations of the $Mn_2^{II,III}$ and $Mn_2^{III,IV}$ species coexist in the reaction solution mixture, demonstrating that the high oxidation state in the $Mn_2^{III,IV}$ species possesses the desired stability. If we assume that the potential of the III,III/II,III couple of the species we observe under the experimental conditions of flash photolysis is similar to that of the di-μ-acetato complex (0.38 V vs. $Fc^{+/0}$), we can assume a similar potential for the III,IV/III,III couple of the $Mn_2^{III,IV}$ species. We made an analogous estimation of potentials for $[Mn_2(bpmp)(\mu\text{-}OAc)_2]^+$, where the mass spectrometry data indicated formation of $[Mn_2^{III,IV}(bpmp)(\mu\text{-}O)_2]^{2+}$ at potentials close to the III,III/II,III couple of the parent complex.[18] This compression of multiple redox reactions in a narrow potential range, which is a consequence of the ligand exchange reactions, indicates that disproportionation of III,III intermediates might contribute to the formation of the $Mn_2^{III,IV}$ species.

The $Mn_2^{III,IV}$ species reached a maximum concentration of about 10% relative to the initial $Mn_2^{II,III}$ signal before it started to decrease after about 100 flashes (Figure 10). The $Mn_2^{III,IV}$ spectrum was not immediately replaced by any other EPR-active species, suggesting that the $Mn_2^{III,IV}$ complex was further oxidised to an EPR-silent product. This could be either a $Mn_2^{IV,IV}$ complex or a $Mn_2^{III,IV}L^{\cdot}$ form with a ligand-based radical strongly coupled to the metal. Subsequent oxidation could also account for the relatively low yield of $Mn_2^{III,IV}$ species. When the $Mn_2^{III,IV}$ signal was almost fully depleted, a weak radical signal could be observed (Figure 9, in the centre of spectrum d) that was about 70 G wide (peak-to-trough) and had enhanced relaxation properties, as a consequence of being close to a paramagnetic metal centre. It is similar to the radical spectrum observed upon oxidation of the analogous $[Mn_2(bhpp)(OAc)_2]$ complex[21] and most likely arises from the oxidised *tert*-butyl-substituted phenol group. If it is the case that further oxidation of the $Mn_2^{III,IV}$ species results in formation of $Mn_2^{III,IV}L^{\cdot}$, the detected radical signal might arise from a minor fraction of the product where the oxidised phenol ligand has been detached from the manganese, while the major fraction with the radical coordinated to the metal centre is EPR-silent. The disappearance of the $Mn_2^{III,IV}$ EPR species cannot be explained by disintegration of the complexes, as that usually results in the release of monomeric Mn^{II}. In contrast, only a small quantity of Mn^{II} (about 2% of the total Mn concentration) was released according to its EPR signal consisting of six lines at $g = 2$ (Figure 9, spectrum e).[43]

In summary, the results of photo-oxidation show that oxidation of **5** in partly aqueous solution generates a $Mn_2^{III,IV}$ complex, most likely with a di-μ-oxo or di-μ-oxo/hydroxo bridging motif replacing the acetate ligands. In addition, our data indicate that further photoinduced oxidation of this complex might result in a $Mn_2^{IV,IV}$ or $Mn_2^{III,IV}$-$L^{\cdot}$ product.

Conclusions

The unsymmetric ligand in the mixed-valent manganese complex **5** ($[Mn_2^{II,III}L(\mu\text{-}OAc)_2]ClO_4$) provides, together with the bridging acetates, a N_3O_3 and a N_2O_4 donor set to the Mn^{II} and Mn^{III} centres respectively. Compared to the symmetric ligand analogues bpmp[16] and bhpp,[21] the unsymmetric ligand provides an intermediate O/N ratio and substantially stabilises the mixed-valence state, where the higher-valent metal ion is localised in the N_3O_3 environment. The pseudo-octahedral coordination geometry is largely distorted and conversion to the isovalent states is associated with large inner reorganisation energies resulting in slow electron transfer reactions.

Complex **5** displays two oxidation processes in nonaqueous solvents, where charge accumulation precludes the formation of stable oxidation states beyond the $Mn_2^{III,III}$ state. This situation changes in aqueous media where the acetate bridges of **5** are replaced by water-derived ligands. These provide charge compensation by deprotonation upon oxidation of the metal centres.[18,44] As a result, the potential interval for accumulative oxidations becomes more compressed, so that three metal-centred oxidation processes can be driven by $[Ru^{III}(bpy)_3]^{3+}$ ($E_{1/2}$ = 1.27 V vs. NHE). Moreover, the ability to acquire water-derived ligands is an essen-

tial characteristic of any functional model for the water-oxidising complex in PSII.

The product of the photoinduced oxidation is a $Mn_2^{III,IV}$ complex, which can be further oxidised to, most likely, a $Mn_2^{IV,IV}$ complex. The high-valent complexes are oxo- or hydroxo-bridged, which is supported by the EPR spectrum observed for the $Mn_2^{III,IV}$ complex, which is consistent with a strongly antiferromagnetically coupled complex.

These results demonstrate that four, possibly five, manganese valence states can be sustained in the same binucleating ligand, as the build-up of charge can be balanced because of the flexibility of the bridging motif. Water oxidation in PSII is believed to involve at least Mn^{IV} or even Mn^{V} to provide sufficiently electrophilic oxo ligands that can engage in O–O bond formation.[5,7,45] Compared to the related $[Mn_2(bpmp)(OAc)_2]^+$ we note that the increased O/N ratio of **5** stabilises higher valence states, which results in oxidation of the ligand exchange products beyond the $Mn_2^{III,IV}$ level. This is a significant improvement in view of prospective biomimetic water oxidation catalysts. It is however important to note that there is an unavoidable trade-off between stabilising higher oxidation states and maintaining sufficient oxidising potential. For the $Mn_2^{III,IV}$ complex derived from **5** the estimated oxidation potential of the III,IV/III,III couple is probably comparable to the III,III/II,III couple of the parent complex (≈0.4 V vs. $Fc^{+/0}$, ≈0.8 V vs. NHE). This suggests that all oxidation products derived from **5** are within a desirable potential range with respect to the average potential of 0.81 V versus NHE (at pH 7) required for water oxidation. Thus, the O/N ratio in **5** seems to create close to an optimal balance between oxidising potential and valence state stabilisation.

Experimental Section

Materials: 2-(Chloromethyl)-6-formyl-4-methylphenol,[27] dipicolylamine[28] and (3,5-di-*tert*-butyl-2-hydroxybenzyl)(2-pyridylmethyl)amine[21] were prepared according to the literature procedures. Dichloromethane and triethylamine were distilled under argon over sodium/benzophenone and calcium hydride, respectively. Column chromatography was performed using silica gel (60–80 mesh). All other reagents were of reagent grade quality and used as received. ^{1}H NMR spectra were recorded with a Varian 400-MHz spectrometer.

2-{[(3,5-Di-*tert*-butyl-2-hydroxybenzyl)(pyrid-2-ylmethyl)amino]-methyl}-6-formyl-4-methylphenol (2): (3,5-Di-*tert*-butyl-2-hydroxybenzyl)(pyrid-2-ylmethyl)amine (1.64 g, 5.0 mmol) and triethylamine (0.62 g, 6.1 mmol) in CH_2Cl_2 (15 mL) under argon were added to a solution of 2-(chloromethyl)-6-formyl-4-methylphenol (**1**) (1.03 g, 5.6 mmol) in CH_2Cl_2 (15 mL). The reaction mixture was refluxed overnight under argon. The reaction was poured into water and extracted with CH_2Cl_2. The combined organic phases were dried with anhydrous sodium sulfate, filtered and evaporated under reduce pressure. The residue was purified by column chromatography, eluting with CH_2Cl_2/MeOH, 97:3. Yield 1.84 g (95%). ^{1}H NMR ($CDCl_3$): δ = 1.26 (s, 9 H), 1.42 (s, 9 H), 2.28 (s, 3 H), 3.77 (s, 2 H), 3.79 (s, 2 H), 3.84 (s, 2 H), 6.86 (d, 1 H), 7.16–7.20 (m, 2 H), 7.28–7.34 (m, 3 H), 7.65 (dt, 1 H), 8.56 (dd, 1 H), 9.95 (s, 1 H), 10.9 (s broad, 2 H) ppm.

2-{[(3,5-Di-*tert*-butyl-2-hydroxybenzyl)(pyrid-2-ylmethyl)amino]-methyl}-6-(hydroxymethyl)-4-methylphenol (3): Complex **2** (0.94 g, 2.0 mmol) was dissolved in methanol (20 mL) and treated with sodium borohydride (0.17 g, 4.4 mmol). The reaction was stirred at room temperature overnight. The solution was evaporated under reduced pressure and the residue was dissolved in water, acidified to pH 2–3 and stirred for 1 h. The pH was adjusted to 7–8 with sodium hydrogen carbonate and then extracted with dichloromethane. The combined organic phases were washed with brine, dried with anhydrous sodium sulfate and filtered. Evaporation under reduced pressure of the solvent afforded 0.92 g of **3** (97%). ^{1}H NMR ($CDCl_3$): δ = 1.27 (s, 9 H), 1.41 (s, 9 H), 2.24 (s, 3 H), 3.77 (s, 2 H), 3.78 (s, 2 H), 3.85 (s, 2 H), 4.68 (s, 2 H), 6.84 (d, 1 H), 8.90 (d, 1 H), 6.96 (d, 1 H), 7.17 (d, 1 H), 7.22 (d, 1 H), 7.32 (dt, 1 H), 7.74 (dt, 1 H), 8.86 (dd, 1 H), 10.80 (s broad, 2 H) ppm.

2-{[Bis(pyrid-2-ylmethyl)amino]methyl}-6-{[(3,5-di-*tert*-butyl-2-hydroxybenzyl)(pyrid-2-ylmethyl)amino]methyl}-4-methylphenol, H_2L (4): Complex **3** (2.27 g, 4.8 mmol) was dissolved in freshly distilled thionyl chloride (5 mL) and CH_2Cl_2 (30 mL). The solution was stirred at room temperature for 2.5 h and then distilled under reduced pressure. The residue was dissolved in CH_2Cl_2 and washed with a cooled sodium hydrogen carbonate solution. The organic phase was dried with anhydrous sodium sulfate, filtered and evaporated under reduced pressure. The residue was dissolved in CH_2Cl_2 and added to a solution of bis-picolylamine (0.95 g, 4.8 mmol) and triethylamine (1.03 g, 10 mmol) and refluxed overnight under argon. The solution was washed with brine and dried with anhydrous sodium sulfate. After filtration and evaporation under reduced pressure the crude product was purified by column chromatography on silica gel, eluting with CH_2Cl_2/MeOH, 95:5. Yield 2.10 g (67%). ^{1}H NMR ($CDCl_3$): δ = 1.25 (s, 9 H), 1.38 (s, 9 H), 2.19 (s, 3 H), 3.73 (s, 2 H), 3.79 (s, 2 H), 3.82 (s, 2 H), 3.83 (s, 2 H), 3.86 (s, 4 H), 6.79 (d, 1 H), 6.84 (d, 1 H), 6.96 (d, 1 H), 7.06–7.15 (m, 4 H), 7.34 (d, 2 H), 7.42 (d, 2 H), 7.51–7.59 (m, 3 H), 8.49 (d, 1 H), 8.58 (d, 1 H), 10.90 (s broad, 2 H) ppm.

$Mn_2L(OAc)_2{\cdot}ClO_4$ (5): $Mn(OAc)_3{\cdot}(H_2O)_2$ (1.04 g, 3.9 mmol) was added to an ethanol solution (9 mL) of **4** (1.05 g, 1.6 mmol) in one portion. The dark red-brown solution was heated to 60 °C under argon for 20 min. A solution of $NaClO_4{\cdot}H_2O$ (0.58 g, 4.1 mol) in ethanol/water (3:1, 4 mL) was added dropwise and the reaction solution was slowly cooled to room temperature and then stored in a freezer (–18 °C) for 48 h. The dark red-brown microcrystalline solid was filtered and washed with cooled ethanol and diethyl ether. The solid was recrystallised from ethanol/hexane to give 0.79 g dark red-brown rod-like crystals (yield 52%) suitable for X-ray diffraction. ESI-MS: (*m*/*z*) (%) = 883.3354 $[M - ClO_4]^+$. $C_{46}H_{55}N_5O_6Mn_2^+$ (883.2913): found C 56.03, H 5.71, N 7.08, Cl 3.48, Mn 11.05. $C_{46}H_{55}Mn_2N_5O_6{\cdot}ClO_4$: calcd. C 56.19, H 5.64, N 7.12, Cl 3.61, Mn 11.17.

X-ray Crystallography: Single crystal X-ray diffraction patterns were recorded with a Stoe IPDS diffractometer on a rotating anode Mo-radiation source (λ = 0.71073 Å) with &phis; scans of 1° width. The total rotation range was 200°. The sample-detector distance was 70 mm and with the diameter of the image plate being 180 mm this gave max $2\theta \approx 52°$. Measuring further out in 2θ proved to give very little significant extra data. Suitable single crystals were chosen from the crystallisation (see "Synthesis" above) and were mounted and measured inside sealed glass capillaries with mother liquor surrounding the crystals. Crystals that were simply glued to a glass pin ceased to diffract after a few minutes. Indexing, cell refinements and integration of reflection intensities were performed with STOE IPDS software (Stoe & Cie GmbH, Darmstadt). Numerical ab-

sorption correction was performed with the program X-RED (Stoe & Cie GmbH, Darmstadt) and the crystal shape was verified with the program X-SHAPE (Stoe & Cie GmbH, Darmstadt) using multiple measurements of symmetry equivalent reflections. The structure was solved by direct methods using SHELXS97 giving electron density maps where most non-hydrogen atoms could be resolved.[46] The rest of the non-hydrogen atoms were located from difference electron density maps and the structure model was refined with full-matrix least-squares calculations on F^2 using the program SHELXL97-2.[47] All non-hydrogen atoms were refined with anisotropic displacement parameters and the hydrogens, which were placed at geometrically calculated positions and let to ride on the atoms they were bonded to, were given isotropic displacement parameters calculated as $\xi \cdot U_{eq.}$ for the non-hydrogen atoms with $\xi = 1.5$ for methyl H atoms ($-CH_3$) and $\xi = 1.2$ for methylenic ($-CH_2-$) and aromatic H atoms.

Only 39.2% of the reflections fulfilled the significance criterion $I > 2\sigma(I)$, thus the residual values calculated from all reflection are larger than those calculated from the significant reflections.

CCDC-256953 contains the supplementary crystallographic data for this paper. These data can be obtained free of charge from The Cambridge Crystallographic Data Centre via www.ccdc.cam.ac.uk/data_request/cif.

Magnetic Susceptibility: The magnetic susceptibility in the temperature range 4–300 K was measured on a powder sample of **5** at a magnetic field of 1.35 T using a Faraday balance. Correction for diamagnetism was made using Pascal's constants.

Electrochemistry: All solutions were prepared from dry acetonitrile (Merck, spectroscopy grade, dried with MS 3 Å) with 0.1 M tetrabutylammonium perchlorate that had been dried in a vacuum at 353 K (Fluka, electrochemical grade) as the supporting electrolyte. Before all measurements, oxygen was removed by bubbling the stirred solutions with solvent-saturated argon and the samples were kept under argon during measurements. Cyclic voltammetry, differential pulse voltammetry and controlled potential electrolysis were carried out using an Autolab PGSTAT 100 potentiostat with a GPES 4.9 electrochemical interface (Eco Chemie). The working electrode was a glassy carbon disc (diameter 3 mm, freshly polished) for voltammetry, a Pt disk microelectrode (CH Instruments, diameter 25 μm, freshly polished with alumina 0.3 μm) for fast voltammetry or a platinum grid for bulk electrolysis. A platinum spiral in a compartment separated from the bulk solution by a fritted disk was used as the counter electrode. The reference electrode was a nonaqueous Ag/Ag^+ electrode (CH Instruments, 0.01 M $AgNO_3$ in acetonitrile) with a potential of –0.08 V versus the ferrocenium/ferrocene (Fc^+/Fc) couple in acetonitrile as an external standard. All potentials reported here are versus the Fc^+/Fc couple, which is obtained by adding –0.08 V to the potentials measured versus the Ag/Ag^+ electrode. No compensation for iR drop has been made. With a specific conductivity of $\kappa > 0.01\ S\,cm^{-1}$ of the electrolyte the resistance for the microelectrode ($r = 12.5$ μm) is $R = 1/(4\kappa r) < 20$ kΩ With voltammetric peak currents $i < 100$ nA, the iR drop is negligible (<2 mV) in the microelectrode measurements. Digital simulations of the cyclic voltammograms have been performed with GPES 4.9 software (Eco Chemie). The simulated voltammograms have been composed from the faradic current of a quasireversible and a two-component quasireversible model superimposed on a linear nonfaradic background. The heterogeneous electron transfer rate constants are reported as apparent standard rate constants without corrections for double-layer effects.

UV/Vis Spectroscopy: The electronic absorption spectrum was recorded with a UV/Vis-NIR spectrophotometer (Varian CARY 2400) between 200 and 2700 nm. Spectroelectrochemical measurements were made in a OTTLE-type quartz cell with an optical path length of 1 mm. A platinum grid with a size of $10 \times 30\ mm^2$ and 400 meshes per cm^2 was used as the working electrode. The counter and reference electrodes were of the same type as described in the electrochemistry paragraph. Samples were bubbled for 20 min with solvent-saturated argon and transferred to the argon-flushed cell with the argon stream. The spectra were recorded with a UV/Vis diode array spectrophotometer (Hewlett Packard 8435) with the background collected on electrolyte solution in the potential free OTTLE cell.

IR Spectroscopy: IR absorption spectra were recorded at a resolution of $1\ cm^{-1}$ with a Bruker FTIR spectrometer (IFS 66v/S) with the sample as a KBr pellet or as solution in a liquid-sample cell (Bruker A140) between CaF_2 windows and with a path length of 125 μm. The solutions were prepared in CD_3CN (Aldrich, 99.8 atom-% D) or mixtures of CD_3CN with D_2O (Aldrich, 99 atom-% D).

The ratio of free versus coordinated acetate ($R = [OAc^-]/[M\text{-}OAc]$) was determined from the absorbance at $1590\ cm^{-1}$ $\{Abs_{1590} = d(\varepsilon_{OAc^-}[OAc^-] + \varepsilon_{M\text{-}OAc}[M\text{-}OAc]) = d\varepsilon[OAc]\}$ as

$$R = (\varepsilon_{M\text{-}OAc} - \varepsilon)/(\varepsilon - \varepsilon_{OAc^-})$$

where ε is a formal extinction coefficient and $[OAc] = 2 \times [\mathbf{5}]$ is the total acetate concentration. The concentration of free acetate is then given by

$$[OAc^-] = \{1 - 1/(R + 1)\}[OAc]$$

For Reaction (9) the equilibrium constant is defined as

$$K_9 = \{[Mn_2L(OAc)(H_2O)_2]\ [OAc^-])/([Mn_2L(OAc)_2]\ [H_2O]^2\} = [OAc^-]^2/\{([\mathbf{5}] - [OAc^-])\ [H_2O]^2\}$$

and was determined from a plot of $[OAc^-]^2/([\mathbf{5}] - [OAc^-])$ over $[H_2O]^2$.

IR spectroelectrochemical measurements were performed on solutions of **5** in CD_3CN or CD_3CN/D_2O with KPF_6 (0.1 M). The spectra were recorded in a thin-layer cell equipped with CaF_2 windows and an optical path length of 90 μm. The working electrode was a carbon fibre mesh (49% open area) and the counter electrode was a Pt cylinder concentric with the working electrode. The reference electrode was of the same type as described for electrochemistry and connected to the cell by a salt bridge (0.5 M KPF_6 in CD_3CN). CD_3CN, D_2O and KPF_6 were purchased from Sigma Aldrich. CD_3CN was dried with molecular sieves (3 Å) prior to use and KPF_6 was dried overnight at 353 K in vacuo.

EPR Spectroscopy: The electrochemical preparation of EPR samples was performed by bulk electrolysis of 1-mM solutions at controlled potentials. After electrolysis, 250-μL samples were taken with an argon-filled syringe via a septum from the electrolysis vessel and transferred to argon-flushed EPR tubes. The samples were immediately frozen and kept in liquid nitrogen. X-band EPR measurements were performed at cryogenic temperatures with a Bruker E500 ELEXSYS spectrometer equipped with a TE_{102} resonator, an Oxford Instruments ESR 900 flow cryostat and an ITC 503 temperature controller.

For flash photolysis, a 1-mM solution of **5** in dry acetonitrile was mixed at a 1:1 ratio with an aqueous solution containing tris(2,2′-bipyridyl)dichloro-ruthenium(II) hexahydrate ($[Ru^{II}(bpy)_3]^{2+}$) (8 mM), and penta-aminechlorocobalt(III) chloride ($[Co^{III}(NH_3)_5Cl]^{2+}$) (16 mM), as described previously.[32] The solution was transferred to EPR tubes and the samples were immediately frozen in an ethanol/dry ice bath ($T = 198$ K) and then frozen at 77 K. All

sample mixing and handling took place under dim red light and inert atmosphere, and care was taken to minimise the interval between mixing and freezing of the samples (mix–freeze time < 1 min). Laser flashes from a frequency doubled Spectra Physics DCR 3G Nd:YAG laser at 5 Hz and 532 nm (6 ns pulse width, about 250 mJ flash^{-1}) were given at room temperature to the pre-thawed EPR samples. The incident laser light was adjusted with lenses to cover the entire EPR sample volume. After the designated number of flashes, the sample was frozen in an ethanol/dry ice bath within 2 s and then quickly transferred to liquid N_2 until further use. X-band EPR spectra were recorded before and after flash illumination of the EPR samples. Evaluation of the change in $Mn_2^{II,III}$ concentration was done by double integration of the ground-state EPR signal at 4 K, and comparison with a reference $Mn_2^{II,III}$ spectrum from a known concentration of **5** in acetonitrile. To quantify the formation of Mn_2(III,IV) we used $Mn_2^{III,IV}(bpy)_4(\mu\text{-}O)_2$ as spectroscopic reference.[48] The concentration of $Mn_2^{III,IV}(bpy)_4(\mu\text{-}O)_2$ in acetonitrile was determined by UV/Vis spectrophotometry, using the extinction coefficient $\varepsilon = 900\ M^{-1}cm^{-1}$ at λ = 687 nm. Simulations of EPR spectra were made using the Xsophe-Sophe-Xepr-View® software suite from Bruker GmbH.

Supporting Information (see footnote on the first page of this article): Figure S1 shows IR spectroelectrochemistry of **5**. IR spectra of **5** in KBr, and of the isovalent products $[Mn_2^{II,II}L(\mu\text{-}OAc)_2]$ and $[Mn_2^{III,III}L(\mu\text{-}OAc)_2]^{2+}$ in [D_3]acetonitrile solution. Selected crystallographic data not shown in Table 1.

Acknowledgments

This work was supported by grants from the Swedish Energy Agency, The Knut and Alice Wallenberg Foundation, The Swedish Research Council, NEST-STRP SOLAR-H (EU contract no. 516510), The Royal Swedish Academy of Sciences (A. M.), the Carl Trygger Foundation (A. M.), the Swedish Foundation for Strategic Research (M. F. A.) and Stiftelsen Bengt Lundqvists minne (P. H.).

[1] IR spectroelectrochemistry of **5**: a) J. H. Alstrum-Acevedo, M. Kyle Brennaman, T. J. Meyer, *Inorg. Chem.* **2005**, *44*, 6802–6827; b) S. Chakraborty, T. J. Wadas, H. Hester, R. Schmehl, R. Eisenberg, *Inorg. Chem.* **2005**, *44*, 6865–6878.

[2] a) J. H. A. Nugent (Ed.), *Special Issue on Photosynthetic Water Oxidation*, *BBA-Bioenergetics*, Elsevier, Amsterdam, **2001**, p. 1503; b) J. Barber, *BBA-Bioenergetics* **2004**, *1655*, 123–132.

[3] a) B. A. Diner, G. T. Babcock, in *Oxygenic Photosynthesis: The Light Reactions* (Eds.: D. R. Ort, C. F. Yocum), Kluwer Academic Publishers, Dordrecht, **1996**, pp. 213–247; b) J. Barber, *Curr. Opin. Struct. Biol.* **2002**, *12*, 523–530; c) R. D. Britt, in *Oxygenic Photosynthesis: The Light Reactions* (Eds.: D. R. Ort, C. F. Yocum), Kluwer Academic Publishers, Dordrecht, **1996**, pp. 137–164.

[4] a) K. N. Ferreira, T. M. Iverson, K. Maglaoui, J. Barber, S. Iwata, *Science* **2004**, *303*, 1831–1838; b) B. Loll, J. Kern, W. Saenger, A. Zouni, J. Biesiadka, *Nature* **2005**, *438*, 1040–1044.

[5] W. C. Hoganson, G. T. Babcock, *Science* **1997**, *277*, 1953–1956.

[6] a) B. Kok, B. Forbush, M. McGloin, *Photochem. Photobiol.* **1970**, *11*, 457–475; b) B. Forbush, B. Kok, M. McGloin, *Photochem. Photobiol.* **1971**, *14*, 307–321.

[7] M. Haumann, P. Liebisch, C. Müller, M. Barra, M. Grabolle, H. Dau, *Science* **2005**, *310*, 1019–1021.

[8] a) S. Mukhopadhyay, S. K. Mandal, S. Bhaduri, W. H. Armstrong, *Chem. Rev.* **2004**, *104*, 3981–4026; b) J. H. Robblee, R. M. Cinco, V. K. Yachandra, *BBA-Bioenergetics* **2001**, *1503*, 7–23; c) H. Dau, L. Iuzzolino, J. Dittmer, *BBA-Bioenergetics* **2001**, *1503*, 24–39; d) D. Kuzek, R. J. Pace, *BBA-Bioenergetics* **2001**, *1503*, 123–137.

[9] M. Haumann, C. Müller, P. Liebisch, L. Iuzzolino, J. Dittmer, M. Grabolle, T. Neisius, W. Meyer-Klaucke, H. Dau, *Biochemistry* **2005**, *44*, 1894–1908.

[10] a) Y. Naruta, M. Sasayama, T. Sasaki, *Angew. Chem. Int. Ed. Engl.* **1994**, *33*, 1839–1841; b) M. Watkinson, A. Whiting, C. A. McAuliffe, *J. Chem. Soc., Chem. Commun.* **1994**, *18*, 2141–2142; c) W. Ruettinger, M. Yagi, K. Wolf, S. Bernasek, G. C. Dismukes, *J. Am. Chem. Soc.* **2000**, *122*, 10353–10357.

[11] a) J. Limburg, J. S. Vrettos, L. M. Liable-Sands, A. C. Rheingold, R. H. Crabtree, G. W. Brudvig, *Science* **1999**, *283*, 1524–1527; b) A. K. Poulsen, A. Rompel, C. J. McKenzie, *Angew. Chem. Int. Ed.* **2005**, *44*, 6916–6920.

[12] a) L. Sun, H. Berglund, R. Davydov, T. Norrby, L. Hammarström, P. Korall, A. Börje, C. Philouze, K. Berg, A. Tran, M. Andersson, G. Stenhagen, J. Mårtensson, M. Almgren, S. Styring, B. Åkermark, *J. Am. Chem. Soc.* **1997**, *119*, 6996–7004; b) A. Magnuson, Y. Frapart, M. Abrahamsson, O. Horner, B. Åkermark, L. Sun, J.-J. Girerd, L. Hammarström, S. Styring, *J. Am. Chem. Soc.* **1999**, *121*, 89–96; c) L. Sun, L. Hammarström, B. Åkermark, S. Styring, *Chem. Soc. Rev.* **2001**, *30*, 36–49.

[13] L. Sun, M. Raymond, A. Magnuson, D. LeGourrierec, M. Tamm, M. Abrahamsson, P. Huang Kenéz, J. Mårtensson, G. Stenhagen, L. Hammarström, S. Styring, S. Åkermark, *J. Inorg. Biochem.* **2000**, *78*, 15–22.

[14] M. Borgström, N. Shaikh, O. Johansson, M. F. Anderlund, S. Styring, B. Åkermark, A. Magnuson, L. Hammarström, *J. Am. Chem. Soc.* **2005**, *127*, 17504–17515.

[15] a) I. Vass, S. Styring, *Biochemistry* **1991**, *30*, 830–839; b) C. Tommos, G. T. Babcock, *BBA-Bioenergetics* **2000**, *1458*, 199–219; c) P. Geijer, F. Morvaridi, S. Styring, *Biochemistry* **2001**, *40*, 10881–10891; d) R. Radmer, G. Cheniae, *Top. Photosynthesis* **1977**, *2*, 303–348.

[16] a) bpmp = 2,6-bis{[*N*,*N*-bis(2-pyridinemethyl)amino]methyl}-4-methylphenol; b) H. Diril, H. R. Chang, M. J. Nilges, X. H. Zhang, J. A. Potenza, H. J. Schugar, S. S. Isied, D. N. Hendrickson, *J. Am. Chem. Soc.* **1989**, *111*, 5102–5114.

[17] P. Huang, A. Magnuson, R. Lomoth, M. Abrahamsson, M. Tamm, L. Sun, B. van Rotterdam, J. Park, L. Hammarström, B. Åkermark, S. Styring, *J. Inorg. Biochem.* **2002**, *91*, 159–172.

[18] G. Eilers, C. Zettersten, L. Nyholm, L. Hammarström, R. Lomoth, *Dalton Trans.* **2005**, 1033–1041.

[19] P. Huang, J. Högblom, M. F. Anderlund, L. Sun, A. Magnuson, S. Styring, *J. Inorg. Biochem.* **2004**, *98*, 733–745.

[20] bpy = 2,2-bipyridine.

[21] a) bhpp = 2,6-bis{[(2-hydroxy-3,5-di-*tert*-butylbenzyl)(2-pyridylmethyl)amino]methyl}-4-methylphenol; b) R. Lomoth, P. Huang, J. Zheng, L. Sun, L. Hammarström, B. Åkermark, S. Styring, *Eur. J. Inorg. Chem.* **2002**, 2965–2974.

[22] C. Higushi, H. Sakiyama, H. Okawa, R. Isobe, D. E. Fenton, *J. Chem. Soc., Dalton Trans.* **1994**, *7*, 1097–1103.

[23] B. C. Dave, R. S. Czernuszewicz, *Inorg. Chim. Acta* **1998**, *281*, 25–35.

[24] P. Karsten, A. Neves, A. J. Bortoluzzi, J. Strahle, C. Maichle-Mossmer, *Inorg. Chem. Commun.* **2002**, *5*, 434–438.

[25] a) L. Dubois, D.-F. Xiang, X.-S. Tan, J. Pécault, P. Jones, S. Baudron, L. LePape, J.-M. Latour, C. Baffert, S. Chardon-Noblat, M.-N. Collomb, A. Deronzier, *Inorg. Chem.* **2003**, *42*, 750–760; b) L. Dubois, R. Caspar, L. Jacquamet, P.-E. Petit, M. F. Charlot, C. Baffert, M.-N. Collomb, A. Deronzier, J.-M. Latour, *Inorg. Chem.* **2003**, *42*, 4817–4827.

[26] a) C. Fraser, L. Johnston, A. L. Rheingold, B. S. Haggerty, J. K. Williams, J. Whelan, B. Bosnich, *Inorg. Chem.* **1992**, *31*, 1835–1844; b) R. Hotzelmann, K. Wieghardt, U. Florke, H. J. Haupt, D. C. Weatherburn, J. Bonvoisin, G. Blondin, J.-J. Girerd, *J. Am. Chem. Soc.* **1992**, *114*, 1681–1696; c) P. Karsten, A. Neves, A. J. Bortoluzzi, M. Lanznaster, V. Drago, *Inorg. Chem.* **2002**, *41*, 4624–4626.

[27] E. Lambert, B. Chabut, S. Chardon-Noblat, A. Deronzier, G. Chottard, A. Bousseksou, J. Tuchagues, J. Laugier, M. Bardet, J. M. Latour, *J. Am. Chem. Soc.* **1997**, *119*, 9424–9437.
[28] M. Lubben, B. L. Feringa, *J. Org. Chem.* **1994**, *59*, 2227–2233.
[29] I. D. Brown, D. Altermatt, *Acta Crystallogr., Sect. B: Struct. Sci.* **1985**, *41*, 244–247.
[30] a) R. M. Buchanan, K. J. Oberhausen, J. F. Richardson, *Inorg. Chem.* **1988**, *27*, 971–973; b) H.-R. Chang, S. K. Larsen, P. D. W. Boyd, C. G. Pierpont, D. N. Hendrickson, *J. Am. Chem. Soc.* **1988**, *110*, 4565–4576.
[31] H. Diril, H.-R. Chang, X. Zhang, S. K. Larsen, J. A. Potenza, C. G. Pierpont, H. J. Schugar, S. S. Isied, D. N. Hendrickson, *J. Am. Chem. Soc.* **1987**, *109*, 6207–6208.
[32] G. Aromi, J. Telser, A. Ozarowski, L.-C. Brunel, H.-M. Stoeckli-Evans, J. Krzystek, *Inorg. Chem.* **2005**, *44*, 187–196.
[33] a) S. R. Cooper, G. C. Dismukes, M. P. Klein, M. Calvin, *J. Am. Chem. Soc.* **1978**, *100*, 7248–7252; b) M. Zheng, S. V. Khangulov, G. C. Dismukes, V. V. Barynin, *Inorg. Chem.* **1994**, *33*, 382–387; c) J. S. Bashkin, A. R. Schake, J. B. Vincent, H.-R. Chang, Q. Li, J. C. Huffman, G. Christou, D. N. Hendrickson, *J. Chem. Soc., Chem. Commun.* **1988**, *11*, 700–702; d) G. C. Dismukes, J. E. Sheats, J. A. Smegal, *J. Am. Chem. Soc.* **1987**, *109*, 7202–7203.
[34] P. Huang, N. Shaikh, M. Anderlund, S. Styring, L. Hammarström, *J. Inorg. Biochem.* **2006**, *100*, 1139–1146.
[35] In ref.[34] the spin Hamiltonian $\hat{H} = \beta\,\hat{\mathbf{S}}\cdot\mathbf{g}\cdot\mathbf{B} + \hat{\mathbf{I}}_1\cdot\hat{\mathbf{A}}_1\cdot\hat{\mathbf{S}} + \hat{\mathbf{I}}_2\cdot\hat{\mathbf{A}}_2\cdot\hat{\mathbf{S}}$ was used, resulting in the hyperfine parameters $A_{1,x} = 171\times10^{-4}\ \mathrm{cm}^{-1}$, $A_{1,y} = 148\times10^{-4}\ \mathrm{cm}^{-1}$, $A_{1,z} = 261\times10^{-4}\ \mathrm{cm}^{-1}$ and $A_{2,x} = 55\times10^{-4}\ \mathrm{cm}^{-1}$, $A_{2,y} = 90\times10^{-4}\ \mathrm{cm}^{-1}$, $A_{2,z} = 122\times10^{-4}\ \mathrm{cm}^{-1}$ for manganese 1 and 2 respectively.
[36] a) This is based on the potential of the $[Ru(bpy)_3]^{3/2+}$ couple that is considered to be largely solvent independent and amounts to 0.90 V versus $Fc^{+/0}$ in acetonitrile (1.27 V vs. NHE in water). Potentials in nonaqueous solvents are frequently measured and reported versus the aqueous SCE. This introduces unknown junction potentials, however, and a comparison of such data with potentials obtained in other solvents like water is not meaningful even if the potentials are formally given versus the same reference electrode like SCE or NHE. Independent of this problem, electrochemical potentials are intrinsically solvent dependent and any comparison between data in different solvents can only be approximate; b) I. Rubinstein, A. J. Bard, *J. Am. Chem. Soc.* **1981**, *103*, 512–516.
[37] Electrolysis at 0.92 V appears to be a multielectron process presumably because of the oxidation of degradation products.
[38] R. A. Marcus, *J. Chem. Phys.* **1965**, *43*, 679–701.
[39] a) The outer reorganisation energy of the electrode reaction in acetonitrile solutions ($n = 1.344$, $\varepsilon = 35.94$) was estimated from $\lambda_o = [e^2/(8\pi\varepsilon_o)](1/r - 1/R)(1/n^2 - 1/\varepsilon)$ where $r \approx 5$ Å is the molecular radius and $R(\geq 2r)$ is the distance between the molecule and its image charge; b) A. J. Bard, L. R. Faulkner, in *Electrochemical Methods: Fundamentals and Applications*, 2nd ed., Wiley, New York, **2001**.
[40] M. L. A. Abrahamsson, H. Berglund Baudin, A. Tran, C. Philouze, K. E. Berg, M. K. Raymond-Johansson, L. Sun, B. Åkermark, S. Styring, L. Hammarström, *Inorg. Chem.* **2002**, *41*, 1534–1544.
[41] a) P. J. Pessiki, S. V. Khangulov, G. C. Dismukes, *J. Am. Chem. Soc.* **1994**, *116*, 891–897; b) S. V. Khangulov, P. J. Pessiki, V. V. Barynin, D. E. Ash, G. C. Dismukes, *Biochemistry* **1995**, *34*, 2015–2025; c) T. Howard, J. Telser, V. J. DeRose, *Inorg. Chem.* **2000**, *39*, 3379–3385; d) S. Blanchard, G. Blondin, E. Rivière, M. Nierlich, J.-J. Girerd, *Inorg. Chem.* **2003**, *42*, 4568–4578.
[42] K.-O. Schäfer, R. Bittl, W. Zweygart, F. Lendzian, G. Haselhorst, T. Weyhermüller, K. Wieghardt, W. Lubitz, *J. Am. Chem. Soc.* **1998**, *120*, 13104–13120.
[43] Formation of colloidal MnO_2 was not observed by visual inspection but cannot be excluded.
[44] a) J. E. Sheats, R. S. Czernuszewitcz, G. C. Dismukes, A. L. Rheingold, V. Petrouleas, J.-A. Stubbe, W. H. Armstrong, R. H. Beer, S. J. Lippard, *J. Am. Chem. Soc.* **1987**, *109*, 1435–1444; b) E. M. Boelrijk, S. V. Khangulov, C. G. Dismukes, *Inorg. Chem.* **2000**, *39*, 3009–3019.
[45] J. Limburg, J. S. Vrettos, H. Chen, J. C. de Paula, R. H. Crabtree, G. W. Brudvig, *J. Am. Chem. Soc.* **2001**, *123*, 423–430.
[46] G. M. Sheldrick, *Acta Crystallogr., Sect. A: Found. Crystallogr.* **1990**, *46*, 467–473.
[47] G. M. Sheldrick, *Computer Program for the Refinement of Crystal Structures*, University of Göttingen, **1997**.
[48] R. Manchanda, G. W. Brudvig, R. H. Crabtree, *New J. Chem.* **1994**, *18*, 561–568.

Received: July 19, 2006
Published Online: October 27, 2006

